

# The effect of inclination on vortex-induced vibration of a circular cylinder with a base column

Yuanchuan Liu<sup>1</sup>, Fushun Liu<sup>1\*</sup>, Qing Xiao<sup>2</sup>, Lin Zhou<sup>1\*</sup>

<sup>1</sup>College of Engineering, Ocean University of China, Qingdao, 266100, China

<sup>2</sup>Department of Naval Architecture, Ocean and Marine Engineering,  
University of Strathclyde, Glasgow, G4 0LZ, UK

\*Corresponding authors: [percylui@ouc.edu.cn](mailto:percylui@ouc.edu.cn), [zhoulin@ouc.edu.cn](mailto:zhoulin@ouc.edu.cn)

## Abstract

The vortex-induced vibration (VIV) of an inclined cylinder can be affected by its end condition. This paper numerically investigates the effect of inclination on the VIV of an elastically mounted rigid cylinder with a base column, which derives from a floating offshore wind turbine (FOWT). The numerical methods are validated against an existing VIV study of a finite-length cylinder. Two inclination angles, i.e.  $-5^\circ$  and  $-10^\circ$ , are studied to simulate the relatively small wind-induced inclination experienced by FOWTs. Results from stationary simulations show that differences between the force coefficients of inclined and upright cylinders are rather small. Nevertheless, contrary to the finding from previous VIV studies that the effect of inclination on the response of a cylinder with small inclination angles is limited, the present investigation reveals that the maximum response amplitude of the cylinder increases by about 20% when the inclination angle grows to  $-10^\circ$  due to the presence of the base column. Meanwhile, the inclination leads to a reduction in the width of the lock-in regime. The impacts of inclination are further discussed via forced vibration studies with same oscillation parameters, which show that the upper part of the cylinder is more affected by the inclination compared to the base column with a considerable decrease in the amplitude of lift coefficient. The discrepancies in fluid forces are substantiated by analysing the pressure distribution on specified spanwise sections of the cylinder surface.

**Keywords:** Vortex-induced vibration; inclination effect; base column; lock-in.

## 1 Introduction

Vortex-induced vibration (VIV) of elastically mounted rigid cylinders in flow has received a great deal of attention from both academia and industry due to its scientific and practical significance. Comprehensive reviews have been conducted in various aspects of VIV (Bearman, 1984; Sarpkaya, 2004; Williamson and Govardhan, 2004; Bearman, 2011). The majority of previous VIV studies were devoted to cylinders with their axes oriented to be perpendicular to the incident flow either by experiment (Hover et al., 2004; Morse and Williamson, 2009; Raghavan and Bernitsas, 2011; Bourdier and Chaplin, 2012) or via numerical simulations (Navrose and Mittal, 2013; Zhao, 2015a; Wang et al., 2017; Gsell et al., 2019). However, in real-world scenarios flow can approach a structure at an angle, e.g. an inclined pipeline placed in horizontal current. This angle is referred to as inclination angle  $\theta$  in the present study, which is also known as oblique or yaw angle in existing literatures, and an inclination angle of  $0^\circ$  indicates that flow is perpendicular to the axis of the cylinder.

Many efforts have been made to study the effect of inclination on cylinders. Some researches focused on vortex shedding and flow characteristics for stationary inclined cylinders. Ramberg (1983) described the impacts of the inclination angle on a cylinder using the independence principle (IP) or Cosine Law, which stated that the flow with free-stream velocity  $U$  past a cylinder with an inclination angle  $\theta$  could be regarded as a normal-incidence case with a flow velocity of  $U_n = U \cos \theta$  while the contribution from its axial component could be ignored. Matsuzaki et al. (2004) experimentally studied the flow past an inclined cylinder in a low-noise wind tunnel with a hydrogen bubble method and pointed out that the Strouhal number deviated from the IP at  $\theta > 15^\circ$ . Thakur et al. (2004) found in their experiment that the wake vortices of a stationary cylinder showed a similar quasi-two-dimensional state for  $0^\circ \leq \theta \leq 60^\circ$ . Zhao et al. (2009) carried out direct numerical simulations (DNS) for three-dimensional flow past a stationary cylinder with  $\theta$  ranging from  $0^\circ$  to  $60^\circ$  and concluded that the Strouhal number closely followed the IP. However, the lift coefficient was found to depend on  $\theta$  and the mean drag coefficient at  $\theta > 30^\circ$  was larger than that at  $\theta = 0^\circ$ .

Investigations have also been conducted for the VIV of inclined cylinders regarding their responses in the transverse direction. Ramberg (1983) summarised from VIV experiments of cylinders with  $0^\circ \leq \theta \leq 60^\circ$  that the bounds of the lock-in regime for inclined cylinders were in accordance with their normal-incidence counterparts. Jain and Modarres-Sadeghi (2013) analysed their VIV results from a series of experiments with  $0^\circ \leq \theta \leq 75^\circ$  and argued that the width of the lock-in regime as well as the maximum oscillation amplitude did not correspond well to the IP although the onset of lock-in appeared at the same normalised flow velocity for all inclination angles except for  $\theta = 75^\circ$ . Lucor and Karniadakis (2003) numerically investigated the VIV of an inclined circular cylinder with large inclination angles of  $60^\circ$  and  $70^\circ$ . The transverse response amplitude was found to decrease with increasing  $\theta$ . Hu et al. (2018) experimentally studied the VIV of a square cylinder inclined either upwind or downwind with  $-30^\circ \leq \theta \leq 30^\circ$  and reported that the transverse response amplitude was affected by the direction of inclination as well as the inclination angle. Their finding was in agreement with the experimental results from Franzini et al. (2013) for circular cylinders, which showed that the IP was only valid for  $\theta$  up to  $20^\circ$  and that a further increase in  $\theta$  resulted in a decrease in the maximum response amplitude.

Meanwhile, existing researches on the VIV of finite-length cylinders have showed that the end condition of an upright cylinder had significant impacts on its transverse response. Morse et al. (2008) experimentally studied the VIV of a cylinder with an aspect ratio of  $L/D = 8$ , with  $L$  being the length of the cylinder and  $D$  its diameter. They found that the response amplitude in the lower branch of the cylinder with a free end was noticeably higher compared to that of the cylinder with an endplate attached to its free end and that there was no clear transition between the upper and lower branches when the endplate was removed. Zhao and Cheng (2014) analysed the free end effect on the VIV of a finite-length cylinder with  $L/D$  varying from 1 to 20 using CFD simulations and noted that the vortices generated from the free end affected the response amplitude and frequency of the cylinder even at a high  $L/D$  of 10. By conducting VIV experiments for cylinders with very low aspect ratios of  $0.2 \leq L/D \leq 2$ , Gonçalves et al. (2018) pointed out that the response of the cylinder with  $L/D$  lower than 0.5 was primarily induced by vortex shedding around the free end.

It can then be summarised from the above literature review that the VIV response of a cylinder can be influenced by both inclination and its end condition. In the present study, the effect of inclination on the VIV of an elastically mounted circular cylinder with a concentric base column attached to its free end, as illustrated in Figure 1, is investigated numerically, which has been rarely analysed to the best of the authors' knowledge. As our previous research showed that the presence of the base column resulted in strong three-dimensionality of fluid flow (Liu et al., 2020), it is thus conjectured that even a relatively small inclination angle may greatly affect the flow past the cylinder and consequently its VIV responses. Additionally, the cylinder-base model derives from the DeepCwind semi-submersible platform (Robertson et al., 2014), which is designed for the OC4 floating offshore wind turbine (FOWT) and is displayed in Figure 2. For an FOWT operating in wind, the aerodynamic thrust generated by the wind turbine produces a turning moment (Liu et al., 2019b; Tian et al., 2020), leading to the inclination of the platform known as wind-induced inclination (Antonutti et al., 2014). It is thus expected that this work will contribute to the understanding of vortex-induced motion of FOWTs subjected to environmental loads from wind and current.

The rest of this paper is organised as follows. The geometry of the cylinder is firstly described in Section 2, followed by an introduction to the numerical methods in Section 3. Section 4 then presents the computational model established for the inclined cylinder. A validation test is conducted afterwards in Section 5 to validate the numerical tool and models employed in the present study. Subsequently, in Section 6 the numerical results obtained for the cylinder under various conditions are presented and discussed. Finally, conclusions are drawn in Section 7.

## **2 Problem description**

The geometry of the cylinder with a base column studied in this work is illustrated in Figure 1(a). Using the DeepCwind semi-submersible platform (Robertson et al., 2014) as a reference, a relatively short cylinder with a low aspect ratio of  $L/D = 2$  is investigated, where  $L$  is the overall length of the cylinder and  $D$  is its characteristic diameter. The base column has a diameter of  $D_B = 2D$  and a length of  $L_B = 0.2L$ . An important parameter adopted for VIV studies is the mass ratio  $m^* = m/m_d$ , which is

defined as the ratio of the structure mass  $m$  and the displaced fluid mass  $m_d$ , where  $m_d$  is calculated via  $m_d = \rho\pi(D^2L_C + D_B^2L_B)/4$  with  $\rho$  being fluid density and  $L_C$  the length of the upper part of the cylinder (hereinafter referred to as “upper cylinder”). For floating structures like semi-submersibles (Liu et al., 2019a), their mass ratio  $m^*$  is usually close to unity. Therefore, a low mass ratio of  $m^* = 1$  is utilised in this study.

The cylinder is subjected to a uniform flow with velocity  $U$  and is only allowed to oscillate in the crossflow or transverse direction. The Reynolds number is defined as  $Re = UD/\nu$ , with  $\nu$  denoting kinematic fluid viscosity, and remains constant at  $Re = 300$  throughout this study. The choice of setting  $Re = 300$  is made for two reasons: firstly, the fluid flow at  $Re = 300$  is already in the turbulent regime (Kim and Choi, 2005) as in most real-world applications; secondly, the Navier-Stokes equations can be directly solved at an affordable computational cost, without bringing about potential uncertainties introduced by utilising turbulence models (Wang et al., 2017). It is expected that the results obtained from the present study at a relatively low  $Re$  will help understand the effects of inclination on the VIV response of cylindrical structures in high- $Re$  flow (Zhao and Cheng, 2014). The VIV of the cylinder is simulated for a series of flow speeds or reduced velocities. The reduced velocity  $V_r$  in this study is defined as  $V_r = U/(f_n D)$ , where  $f_n$  is the natural frequency of the cylinder in vacuum. In order to keep  $Re$  the same at different  $V_r$ , only  $f_n$  or equivalently, the stiffness of the spring restraining the cylinder, is adjusted.

The inclination angle  $\theta$  of the cylinder relative to the incident flow is depicted in Figure 1(b). When the cylinder is inclined, a pivot point is firstly defined as the intersection of the cylinder axis and its top side. The cylinder is then rotated about the pivot point in the transverse direction. According to the definition of Franzini et al. (2013), as the bottom of the cylinder is inclined towards the upstream direction, the inclination angle  $\theta$  shown in Figure 1(b) is regarded negative, which corresponds to the environmental condition where the incident wind and current are aligned in the same direction for an FOWT. Existing FOWT studies show that the typical wind-induced inclination angle of the floating platform under normal operating conditions is relatively small, i.e. no more than  $10^\circ$  (Antonutti et al., 2016; Liu et al., 2017). As a result, two small inclination angles, i.e.  $-5^\circ$  and  $-10^\circ$ , are investigated to analyse the

effects of inclination on the VIV of the cylinder with a base column. As the normal component of flow velocity  $U_n$  is very close to  $U$ , e.g.  $U_n \approx 98.5\%U$  for  $\theta = -10^\circ$ , the same definition of reduced velocity  $V_r$  is adopted for both upright and inclined cylinders in the present study. It is worth pointing out that the inclined cylinder is clipped at the pivot point and only the geometry below the horizontal plane is retained to accurately represent the underwater geometry of the cylinder due to inclination. Consequently, the inclined cylinder has the same surface area and displaced fluid mass as its upright counterpart, which facilitates direct comparisons among results from cylinders with different inclination angles.

### 3 Numerical methods

#### 3.1 Flow model

The flow past an oscillating cylinder is governed by the following unsteady, incompressible Navier-Stokes equations formulated in an Arbitrary Lagrangian-Eulerian (ALE) framework:

$$\nabla \cdot \mathbf{U} = 0 \quad (1)$$

$$\frac{\partial \mathbf{U}}{\partial t} + \nabla \cdot [(\mathbf{U} - \mathbf{U}_g)\mathbf{U}] = -\frac{\nabla p}{\rho} + \nu \nabla^2 \mathbf{U} \quad (2)$$

where  $\mathbf{U}$  and  $\mathbf{U}_g$  represent the velocity field of the flow and computational grid, respectively;  $t$  is time;  $p$  stands for the pressure field of the flow;  $\rho$  and  $\nu$  denote fluid density and kinematic viscosity, separately. The effects of free surface and water waves are not considered in the present study.

The flow field is solved using an open source CFD code OpenFOAM version 4.1 (<https://openfoam.org>), which adopts a finite volume approach to discretise the governing equations. OpenFOAM provides a large number of built-in solvers with various functionalities. In the present study, the pimpleDyMFoam solver with a moving mesh capability is selected, where a PIMPLE (merged PISO-SIMPLE) algorithm is applied to deal with the coupling of velocity and pressure. A backward scheme with second-order accuracy is used for temporal discretisation and a second-order upwind scheme is adopted for convective terms. Gradient terms are handled via a second-order Gauss linear scheme.

### 3.2 Structural model

The transverse response of an elastically mounted cylinder subjected to fluid forces can be described via the following equation of motion:

$$m\ddot{y} + c\dot{y} + ky = F_y \quad (3)$$

where  $y$  denotes the transverse motion of the cylinder;  $m$ ,  $c$  and  $k$  represent the cylinder mass, structural damping coefficient and spring stiffness, respectively;  $F_y$  stands for the transverse fluid force exerted upon the cylinder. In this study, structural damping is not considered and thus the damping coefficient  $c$  is set to zero. The Newmark-beta method (Newmark, 1959) is adopted to solve Eq. (3) for the transverse response  $y$  of the cylinder, with the integration coefficients for velocity and displacement set to  $\gamma = 0.5$  and  $\beta = 0.25$ , respectively.

### 3.3 Fluid-structure interaction

The interaction between fluid and the cylinder is handled in a tightly coupled manner, as illustrated in Figure 3. When a simulation starts, the flow field surrounding the cylinder, i.e. fluid velocity and pressure, is initialised. At the beginning of each time step, the fluid force acting on the cylinder is firstly computed by integrating pressure and shear stress over the cylinder surface. The response of the cylinder is then calculated by solving Eq. (3). Subsequently, the computational mesh is updated to accommodate the motion of the cylinder utilising a solid body motion approach, where the overall mesh region moves along with the cylinder to avoid the deterioration of grid quality. The Navier-Stokes equations, i.e. Eq. (1)-(2), are solved afterwards to update the flow field. Within each time step, a number of iterations are performed. At the end of every iteration, flow field convergence is checked, i.e. whether the residuals of all flow field variables drop by three orders of magnitude. If convergence is not achieved, a new iteration begins; otherwise, computation advances to the next time step. The computational procedure is repeated for every time step until the end of the simulation.

## 4 Computational model

### 4.1 Computational domain and boundary conditions

The computational domain established for the present study is shown in Figure 4, where the cylinder is placed in an upright position as an example. The top of the cylinder is located on the top side of the domain and the distance measured from the bottom of the base column to the bottom side of the domain is  $10D$ , in which  $D$  denotes the diameter of the upper cylinder. The centreline of the cylinder is  $20D$  away from the other two sides as well as the *Inlet* boundary, and  $30D$  from the *Outlet* boundary, so as to minimise the impacts of domain boundaries on the fluid flow around the cylinder. For cases with an inclined cylinder, the cylinder is rotated about the pivot point where the cylinder axis intersects the top side of the computational domain while all other boundaries remain unchanged.

The boundary conditions utilised for the computational model are also annotated in Figure 4. A constant flow velocity  $U$  is specified for the fluid velocity  $\mathbf{U}$  in the positive  $x$  direction at the *Inlet* boundary while the fluid pressure  $p$  at the *Outlet* boundary is set to zero. A symmetry condition is applied at the four *Sides*, where the velocity component normal to these boundaries is always zero. The effect of free surface on the fluid flow is not considered in this study. A no-slip condition is imposed on the *Cylinder* boundary so that the fluid velocity  $\mathbf{U}$  on the cylinder surface is equal to the calculated structure velocity  $\mathbf{U}_s$ .

### 4.2 Mesh and time-step size sensitivity tests

A mesh sensitivity test is carried out to ensure that the numerical results obtained in the present study are independent of the computational mesh. Three cases with different mesh density are set up, which are named *Coarse*, *Medium* and *Fine* as listed in Table 1. A structured grid topology is adopted for all three meshes but the number of elements assigned along the circumference of the cylinder increases, thus resulting in a growing overall cell count. The height of the first cell away from the cylinder surface is  $0.004D$  for all grids, which is sufficiently small as was pointed out by Zhao and Cheng (2014) in their VIV study for a similar cylinder with a free end. The computational mesh for the *Medium* grid with an inclination angle of  $\theta = -10^\circ$  is

presented in Figure 5, where Figure 5(a) depicts the mesh on the top side of the computational domain and Figure 5(b) shows the mesh on the cylinder surface. Grid points are deliberately distributed towards the cylinder to better capture vortex shedding as well as the interaction between fluid flow and the structure.

Figure 6 compares the time series of the non-dimensional cylinder response  $y/D$  and lift coefficient  $C_L$  within two periodic response cycles for the three cases at  $\theta = -10^\circ$  and  $V_r = 6$ . It is shown in Figure 6 that the time series curves from the *Medium* and *Fine* meshes nearly coincide, indicating that the mesh density adopted for the *Medium* grid is adequate for the present study. Table 1 further compares  $A_y/D$  and  $C_{L,rms}$  among the three cases, and the difference between the *Medium* and *Fine* cases is found to be smaller compared to that between the *Medium* and *Coarse* cases. Therefore, the *Medium* grid is employed for subsequent simulations.

Similarly, a sensitivity test is conducted for the time-step size  $\Delta t$ . A nondimensional time-step size  $\Delta t/T_v$  is defined by normalising  $\Delta t$  with the vortex shedding period  $T_v$  for a stationary, infinitely long cylinder. According to the definition of the Strouhal number  $St$ ,  $T_v$  can be calculated as  $T_v = D/(St \cdot U)$  while  $St$  is about 0.2 at  $Re = 300$  (Zhao and Cheng, 2014). Three simulations are performed at  $\theta = -10^\circ$  and  $V_r = 6$ , with  $\Delta t/T_v$  set to 1/500, 1/1000 and 1/2000, respectively. Figure 7 shows that the time series of  $y/D$  and  $C_L$  for cases with  $\Delta t/T_v = 1/1000$  and 1/2000 agree very well, which is further corroborated by the slight difference presented in Table 1 for  $A_y/D$  and  $C_{L,rms}$  between the two cases. The time-step size of  $\Delta t = T_v/1000$  is thus adopted in the present study.

## 5 Validation test

The FSI tool adopted for the present study is validated by studying the VIV of a circular cylinder with a low aspect ratio  $L/D$  of 2 at  $Re = 300$ , which was previously investigated by Zhao and Cheng (2014). No base column is attached, and the truncated cylinder has a low mass ratio  $m^*$  of 2 with zero structural damping. The cylinder is only allowed to translate in the transverse direction.

Figure 8 compares the predictions from the present tool with those provided by Zhao and Cheng (2014) at various  $V_r$ . It is found that the results from the two

simulations agree rather well. As is shown in Figure 8(a), the non-dimensional transverse response amplitude  $A_y/D$  of the cylinder reaches its maximum of about 0.75 at  $V_r = 6$  then gradually decreases to 0.25 at  $V_r = 12$ . Figure 8(b) demonstrates that the response frequency ratio  $f/f_n$  becomes close to unity as  $V_r$  increases, while the rms of lift coefficient  $C_{L,rms}$  in Figure 8(c) peaks at  $V_r = 5$  and remains relatively small outside the range of  $4 \leq V_r \leq 7$ . The good agreement between the data obtained from the two studies indicates that the present FSI tool is capable of carrying out VIV simulations of an elastically mounted rigid cylinder with a low aspect ratio.

## 6 Results and discussion

This section presents the results obtained with the FSI tool for the present cylinder with different inclination angles. The effect of inclination on the cylinder and fluid flow is analysed under stationary, free vibration as well as forced vibration conditions.

### 6.1 Flow past a stationary cylinder

The flow past a stationary cylinder is firstly simulated in this section to study the effect of inclination on flow characteristics around the cylinder under the stationary condition. The time series of force coefficients  $C_D$  and  $C_L$  for the cylinder with an inclination angle of  $\theta = 0^\circ$  and  $\theta = -10^\circ$  are shown in Figure 9. A non-dimensional time  $Ut/D$  is defined with the flow velocity  $U$  and the diameter of the upper cylinder  $D$ . The force coefficients are obtained by normalising the in-line and transverse forces  $F_x$  and  $F_y$  via the following formula:

$$C_D, C_L = \frac{F_x, F_y}{0.5\rho U^2 A_p} \quad (4)$$

where  $\rho$  is fluid density;  $U$  is flow velocity;  $A_p$  is the projected area of the cylinder on the plane normal to the flow direction. In order to make it possible for direct comparisons of  $C_D$  and  $C_L$  between cases with different inclination angles, the projected area  $A_p$  for an upright cylinder is adopted in the present study for all cases, which is computed as  $A_p = DL_C + D_B L_B$  (refer to Figure 1(a) for parameter definitions).

It can be seen from Figure 9 that after the initial fluctuations due to transient effects,  $C_D$  remains nearly constant at about 0.9 for both cases. Meanwhile,  $C_L$  stays close to zero throughout the simulations. Although different from the periodically fluctuating

$C_D$  and  $C_L$  normally observed for infinitely long cylinders, the present results are in accordance with the predictions of Zhao and Cheng (2014) for a finite cylinder with an aspect ratio  $L/D$  of 5 and with no base column attached at  $Re = 300$ . As pointed out by Zhao and Cheng (2014), the absence of oscillations in forces is attributed to the presence of a free end, i.e. the base column in this study, which suppresses the periodic vortex shedding present in the flow past an infinitely long cylinder. This is confirmed by visualising the local vorticity field at various spanwise sections perpendicular to the cylinder axis as illustrated in Figure 10(a). A non-dimensional parameter  $z/L$  is defined to determine the location of a section by dividing its axial coordinate  $z$  by the overall length of the cylinder  $L$ , with  $z/L = 0$  being the bottom of the base column and  $z/L = 1$  the top of the cylinder. It is worth pointing out that the sections for an inclined cylinder are also constructed to be parallel to the base column as for its upright counterpart. Figure 11 shows the contours of the axial component of vorticity field  $\omega_z$  at three sections, i.e.  $z/L = 0.1, 0.25$  and  $0.5$ , along the cylinder at  $\theta = -10^\circ$ . It can be seen from Figure 11 that at each section a pair of symmetric shear layers separate from the two sides of the cylinder and stretch out to the downstream of the cylinder, with no asymmetric vortex shedding patterns such as von Kármán vortex streets observed, as was previously reported by Benitz et al. (2016). For the section at  $z/L = 0.25$  shown in Figure 11(b), as it is close to the base column, the pair of shear layers originating from the upper cylinder gradually spread outward and merge with the vortices generated from the upper edge of the base column in the downstream, demonstrating the effect of the base column on the flow around the upper cylinder.

Although the results of the total force coefficients are very close for the two cases at  $\theta = 0^\circ$  and  $\theta = -10^\circ$ , a close examination of the local flow field around the cylinder reveals that the flow is affected by the inclination of the cylinder. Figure 12 compares the three-dimensional vortex structure represented by the iso-surface of  $Q = 0.2$ , where  $Q$  is the second invariant of the rate of strain tensor. Detailed descriptions of the vortex structure around a stationary upright cylinder with a base column placed in a uniform flow have been provided in our previous paper (Liu et al., 2020), and thus only the differences between the two cases are discussed here. For the case with an inclination angle of  $\theta = -10^\circ$ , it is found that the vortex structure generated from the sharp upper

edge of the base column expands and influences the upper cylinder to an even larger extent than for  $\theta = 0^\circ$ , as marked by the black ellipse in Figure 12. This is further substantiated in Figure 13 by comparing the distribution of pressure coefficient  $C_p$  at same sections between the two cases. The pressure coefficient  $C_p$  is calculated as:

$$C_p = \frac{p - p_\infty}{0.5\rho U^2} \quad (5)$$

where  $p$  is the measured pressure at a given location on the cylinder;  $p_\infty$  is the reference pressure in the far field and is set to zero in the present study. The same three sections studied earlier are analysed, i.e.  $z/L = 0.1, 0.25$  and  $0.5$ . For a given section, an azimuth angle  $\beta$  is defined in Figure 10(b), which is measured from the stagnation point on the front side of the cylinder in the clockwise direction. As the vortex structure around the cylinder is symmetric as previously demonstrated, Figure 13 only shows the distribution of  $C_p$  on half of the sections with  $\beta$  ranging from  $0^\circ$  to  $180^\circ$ . Compared to the upright cylinder, although  $C_p$  on the rear side of the inclined cylinder barely changes, differences are observed on the front side, especially at  $z/L = 0.25$ , where a noticeable decrease in  $C_p$  is present near the stagnation point at  $\beta = 0^\circ$ . Meanwhile,  $C_p$  at  $z/L = 0.1$  increases slightly within  $0^\circ \leq \beta \leq 120^\circ$  due to the presence of inclination. The discrepancies in the vortex structure and the distribution of  $C_p$  along the cylinder between the two cases with different inclination angles thus illustrate the effect of inclination on the fluid flow around the cylinder.

## 6.2 VIV of an elastically mounted cylinder

The VIV of the elastically mounted cylinder with inclination angles of  $\theta = 0^\circ, -5^\circ$  and  $-10^\circ$  is simulated and analysed in this section. A series of simulations with different reduced velocity  $V_r$ , varying from 3 to 12 with an increment of 1, is performed.

### 6.2.1 Motion response

Figure 14(a) compares the variation of the non-dimensional transverse response amplitude  $A_y/D$  with respect to  $V_r$  among the three cases with different inclination angles. It is found for the upright cylinder that  $A_y/D$  jumps steeply from close to zero at  $V_r = 3$  to around 0.6 at  $V_r = 5$ . It then remains above 0.5 until  $V_r = 8$  and gradually decreases to about 0.15 at  $V_r = 12$ . Unlike the response amplitude plots of cylinders

with infinite length or large aspect ratios, a prominent feature of Figure 14(a) is that no distinct upper and lower branches can be identified, which was also observed by Morse et al. (2008) in their experimental study of the effect of end conditions on the VIV of cylinders and was attributed to the presence of free ends. Comparing the results of the upright cylinder with those for the two cases with an inclined cylinder shows that although a similar trend is present, the response of the cylinder is found to be augmented by its inclination in the  $V_r$  range where  $A_y/D$  is the most significant. Meanwhile, as the inclination angle  $\theta$  increases from  $-5^\circ$  to  $-10^\circ$ ,  $A_y/D$  also becomes larger. Specifically, at  $V_r = 6$  where the cylinder response reaches its maximum for all cases,  $A_y/D$  increases considerably from about 0.58 at  $\theta = 0^\circ$  to around 0.69 at  $\theta = -10^\circ$  by nearly 20%. However, the response of the inclined cylinder becomes smaller than that of its upright counterpart at  $V_r$  larger than 9, where a sharp decrease in  $A_y/D$  is present at  $V_r = 10$  for the cylinder with  $\theta = -10^\circ$ . The results presented here show that even with a relatively small inclination angle of  $\theta = -10^\circ$ , the VIV response of the cylinder can be considerably influenced. This is in contrast with the previous finding about the effect of inclination on the VIV of circular cylinders, which stated that the responses of a cylinder with such a small inclination angle should be almost equal to the results of its upright counterpart (Franzini et al., 2013; Zhao, 2015b). The disparities may be attributed to the presence of the base column and the low aspect ratio of the present model, which again stresses the important impacts of end conditions for cylinders.

The response frequency ratio  $f/f_n$ , defined as the ratio of the cylinder response frequency  $f$  and its natural frequency in vacuum  $f_n$ , is plotted in Figure 14(b). In order to calculate the cylinder response frequency  $f$ , a spectral analysis is conducted for the response time series over a non-dimensional duration of  $Ut/D = 100$  and  $f$  is set as the dominant frequency with the greatest spectrum magnitude. As shown in Figure 14(b), for the upright cylinder,  $f/f_n$  increases almost linearly from  $V_r = 4$  to  $V_r = 11$  and passes through the line  $f/f_n = 1$  between  $V_r = 9$  and  $V_r = 10$ . Similar to the response amplitude plots illustrated in Figure 14(a), the characteristic jump in  $f/f_n$  between the upper and lower branches for cylinders with infinite length or large aspect ratios is not present, which again is consistent with the finding of Zhao and Cheng (2014) for a truncated cylinder as well as the experimental results from Morse et al. (2008).

The results for the upright cylinder and the inclined cylinder at  $\theta = -5^\circ$  are similar. However, for the cylinder at  $\theta = -10^\circ$ ,  $f/f_n$  behaves differently within the range of  $9 \leq V_r \leq 11$  and remains close to 1, which will be further discussed in Section 6.2.2.

The  $V_r$  range of the lock-in or synchronisation regime is then determined. The lock-in phenomenon is characterised by large transverse response amplitude. The lower bound of the lock-in regime for the three cases can thus be easily identified from Figure 14(a) as  $V_r = 5$ , where  $A_y/D$  rises significantly. In order to determine the upper bound of the lock-in regime, the definition of lock-in proposed by Williamson and Govardhan (2004) is employed, which states that the frequency of cylinder response should match that of periodic vortex shedding, or equivalently, the frequency of the fluid force exerted on the cylinder. Figure 15 illustrates the time series and power spectral density (PSD) plots of  $y/D$  and  $C_L$  for the VIV of the upright cylinder. Results for two different  $V_r$ , i.e.  $V_r = 11.5$  and  $V_r = 12$ , are analysed, which are presented to demonstrate the transition from the lock-in regime to the desynchronised regime. A smaller increment of 0.5 than the value previously adopted is used to help better identify the upper bound of the lock-in regime. The periodic time series of the response as well as the matching of dominant power spectral density (PSD) frequencies of  $y/D$  and  $C_L$  at  $V_r = 11.5$  indicate that the response of the cylinder is within the lock-in regime. However, the dominant frequency of  $C_L$  at  $V_r = 12$  deviates from that of the response, suggesting that the cylinder response and the fluid force are desynchronised. As a result,  $V_r = 11.5$  is regarded the upper bound of the lock-in regime for the cylinder at  $\theta = 0^\circ$ . Similarly, the results presented in Figure 16 for the cylinder at  $\theta = -5^\circ$  show that the upper bound of the lock-in regime can be determined as  $V_r = 11.5$ , while it is  $V_r = 10$  for the cylinder at  $\theta = -10^\circ$  as demonstrated in Figure 17. It is thus found that the  $V_r$  range of the lock-in regime for the inclined cylinder at  $\theta = -10^\circ$  reduces compared to the results at  $\theta = 0^\circ$  and  $\theta = -5^\circ$ .

### 6.2.2 Force coefficient

Figure 18(a) shows the variation of rms of lift coefficient  $C_{L,rms}$  of the cylinder with different inclination angles with respect to  $V_r$ . For the cylinder at  $\theta = 0^\circ$ ,  $C_{L,rms}$  rises rapidly from nearly zero at  $V_r = 3$  to its maximum of about 0.6 at  $V_r = 5$  and then

gradually decreases to just above zero within  $9 \leq V_r \leq 12$ . For the two inclined cases, the results show a similar trend to that of the upright cylinder. It is worth noting that the maximum  $C_{L,rms}$  increases with the inclination angle  $\theta$ , which is in agreement with the rise of  $A_y/D$  shown in Figure 14(a).

However, unlike the noticeable differences of maximum  $A_y/D$ ,  $C_{L,rms}$  at  $V_r = 6$  for the three cases are very close to each other, which seems rather conflicting at first sight. This can be explained by introducing a relationship between  $A_y/D$  and  $C_{L,rms}$ :

$$A_y/D = \frac{\sqrt{2}}{2\pi^3} \frac{C_{L,rms} V_r^2}{m^* |1 - (f/f_n)^2|} \frac{1 + (D_B/D)(H_B/H_C)}{1 + (D_B/D)^2 (H_B/H_C)} \quad (6)$$

which was derived in our previous paper (Liu et al., 2020) for an upright cylinder with a base column. The third fraction on the right side of Eq. (6) is related to the geometrical properties of the cylinder as illustrated in Figure 1(a) and remain the same for the three cases in the present study. It should be pointed out that the relationship is established based on the assumption that the transverse response  $y$  and force  $F_y$  are both described in a purely sinusoidal form, which is reasonable for  $V_r$  in the lock-in regime.

It is found from Eq. (6) that at given  $V_r$  and  $m^*$ , the response amplitude  $A_y/D$  is determined by both  $C_{L,rms}$  and the response frequency ratio  $f/f_n$ . For the two inclined cylinders at  $V_r = 6$ , although the difference between their  $C_{L,rms}$  and that of the upright cylinder is rather small, a larger  $f/f_n$  shown in Figure 14(b) corresponds to a larger  $1/|1 - (f/f_n)^2|$  and consequently leads to the increase in  $A_y/D$ . Similarly, the drastic decrease of  $A_y/D$  at  $\theta = -10^\circ$  and  $V_r = 10$  in Figure 14(a) can also be explained by an even more insignificant  $C_{L,rms}$  of about 0.003 compared to other conditions even though  $f/f_n$  is very close to unity.

According to Dahl et al. (2010), the response frequency  $f$  of the cylinder is related to an effective added mass  $m_{EA}$  in the following manner:

$$f = \sqrt{\frac{k}{m + m_{EA}}} \quad (7)$$

where the effective added mass  $m_{EA}$  is the equivalent mass associated with the fluid force in phase with cylinder acceleration. By normalising  $m_{EA}$  in the same way as the mass ratio  $m^*$ , an effective added mass coefficient  $C_{EA}$  is defined as  $C_{EA} = m_{EA}/m_d$ ,

where  $m_d$  is the displaced fluid mass. The response frequency ratio  $f/f_n$  can then be represented using  $C_{EA}$  as:

$$f/f_n = \sqrt{1/(1+C_{EA})} \quad (8)$$

Following Khalak and Williamson (1999) and Wang et al. (2019),  $C_{EA}$  in the transverse direction can be calculated as:

$$C_{EA} = \frac{2U^2 C_{L1} \cos \phi_1}{\pi (A_y/D) D^2 (2\pi f)^2} \quad (9)$$

where  $C_{L1}$  and  $\phi_1$  are the magnitude and phase (relative to  $y/D$ ) of the first harmonic of  $C_L$ , separately. The time series of  $C_L$  is analysed via the fast Fourier transform (FFT) to obtain  $C_{L1}$  and  $\phi_1$ . It is worth pointing out that the effective added mass should never be interpreted as a physical mass but rather as a normalised force and that a negative  $C_{EA}$  means the fluid force is out-of-phase with the cylinder response by  $180^\circ$ .

Figure 18(b) shows the variation of  $C_{EA}$  for the cylinder with different inclination angles with respect to  $V_r$  in the lock-in regime. For all three cases, a similar trend is observed, i.e.  $C_{EA}$  decreases as  $V_r$  increases. Correspondingly, according to Eq. (8),  $f/f_n$  will increase along with  $V_r$ , which is in line with the positive correlation between  $f/f_n$  and  $V_r$  as illustrated in Figure 14(b). Meanwhile, at  $V_r = 9$ ,  $C_{EA}$  approaches zero for all cases, which corresponds to  $f/f_n$  being close to unity. However, while  $C_{EA}$  falls below zero at  $V_r = 10$  for the cylinder at  $\theta = 0^\circ$  and  $\theta = -5^\circ$ , it stays positive for the case with  $\theta = -10^\circ$  despite being rather small, which again is consistent with the disparities in  $f/f_n$  among the cases at  $V_r = 10$  and partially explains the noticeable differences in  $A_y/D$ . Additionally, compared to the upright cylinder,  $C_{EA}$  for the two inclined cases is generally noticeably smaller.

Figure 19(a) shows the variation of mean of drag coefficient  $C_{D,mean}$  with respect to  $V_r$  for the cylinder with different inclination angles. It is found that for all three cases  $C_{D,mean}$  show a similar trend to  $A_y/D$  in Figure 14(a), with their maxima occurring at  $V_r = 5$  and  $V_r = 6$ , which indicates that  $C_{D,mean}$  is closely related to  $A_y/D$ . Outside the lock-in regime where the cylinder response is small, i.e. at  $V_r = 3$ ,  $V_r = 4$  and  $V_r = 12$ ,  $C_{D,mean}$  remains close to 0.9 which is the value of  $C_D$  for a stationary cylinder. By contrast,  $C_{D,mean}$  increases significantly within the lock-in regime. Comparing the

results from the three cases reveals that as the inclination angle  $\theta$  increases,  $C_{D,mean}$  becomes larger within  $5 \leq V_r \leq 8$  but drops sharply at  $V_r = 10$  and  $V_r = 11$ , which agrees well with the variation of  $A_y/D$ . The rms of drag coefficient  $C_{D,rms}$  illustrated in Figure 19(b) closely resembles  $C_{D,mean}$  in terms of general trend. Compared to the result of the upright cylinder,  $C_{D,rms}$  at  $\theta = -10^\circ$  almost doubles, reaching a maximum of about 0.26 at  $V_r = 6$  in the lock-in regime. It is thus reasonable to expect noticeable differences in the in-line response of two-degree-of-freedom VIV between an upright cylinder and its inclined counterpart.

### 6.2.3 Fluid flow

The three-dimensional vortex evolution for the inclined cylinder with  $\theta = -10^\circ$  at  $V_r = 6$  is visualised in Figure 20 as an example, attempting to link the fluid flow to the VIV response of the cylinder. Results from seven consecutive instants within one response cycle denoted as ‘a’ - ‘g’ are presented. The complex vortical structures around the cylinder are illustrated by the iso-surfaces of  $Q = 0.2$ . It should be noted that the cylinder is viewed from its bottom and that the side of the cylinder in the positive  $y$  direction is shown. At instant ‘a’, the shear layer separated from the side of the upper cylinder is clearly visible and is found to merge with the vortex generated by the upper edge of the base column. Just after the cylinder moves past its maximum in the positive  $y$  direction at instant ‘b’, the shear layer is shed from the upper cylinder forming a vortex orientated in the spanwise direction while the upper edge vortex still adheres to the base column. Meanwhile, vortex shedding from the side of the base column is not observed possibly due to its relatively short length. The flow then convects the spanwise vortex shed from the upper cylinder to the downstream while the bottom part still clings to the base column, effectively stretching the spanwise vortex in the streamwise direction as shown at instant ‘c’. As the cylinder translates further in the negative  $y$  direction, the spanwise vortex is finally separated from the base column at instant ‘d’ and bends towards the top end of the cylinder, which is likely to be associated with the so-called “upwash velocity” as discussed by Zhao and Cheng (2014). While the spanwise vortex is convected further downstream, another vortex orientated in the streamwise direction is formed from the lee side of upper cylinder and stays close to the base column, as can be observed at instant ‘e’. The streamwise vortex keeps

drawing energy from the near wake of the cylinder and elongates towards the downstream at instant ‘ $f$ ’ before finally separating from the cylinder at instant ‘ $g$ ’.

### 6.3 Forced vibration of an inclined cylinder

The results presented in Section 6.2 show that discrepancies between the cylinders with different inclination angles are present for both  $A_y/D$  and  $f/f_n$  at same  $V_r$ , which makes it difficult to assess the impacts of inclination on fluid flow and fluid forces exerted upon the cylinder. The impacts are then discussed in this section by carrying out forced vibration simulations with same oscillation parameters imposed on the cylinder at  $\theta = 0^\circ$  and  $\theta = -10^\circ$ . The vibration amplitude and frequency are set to  $A_y/D = 0.6$  and  $f/f_n = 0.8$ , respectively, which roughly correspond to the VIV response of the upright cylinder at  $V_r = 6$ . This specific  $V_r$  is selected because the responses are most significant for both cases, as shown in Figure 14(a). It is thus reasonable to expect noticeable differences in fluid forces with the given vibration parameters. Figure 21 illustrates the time series of the forced vibration  $y/D$  over two complete cycles. The letters (‘A’ - ‘H’) annotated in Figure 21 denotes eight consecutive and evenly spaced instants within one vibration cycle.

#### 6.3.1 Force coefficient

Figure 22 compares the time series of  $C_L$  and  $C_D$  over two complete cycles between the two cases under the forced vibration condition. It is easily seen from Figure 22(a) that the variation amplitude of  $C_L$  for the case with  $\theta = -10^\circ$  is considerably smaller than that of the upright cylinder. The comparison suggests that the vibration amplitude for the inclined cylinder would be higher than its upright counterpart if the two cylinders were freely vibrating with  $C_L$  of the same magnitude, which is consistent with the results at  $V_r = 6$  from the free vibration studies. Meanwhile, Figure 22(b) shows that both mean and variation amplitude of  $C_D$  for the cylinder at  $\theta = -10^\circ$  are larger than at  $\theta = 0^\circ$ , which is also in accordance with Figure 19 under the free vibration condition. The results presented in Figure 22 for forced vibration simulations clearly show that the inclination greatly affects the fluid forces acting on the cylinder.

The impacts of inclination on the cylinder are further analysed in Figure 23 by comparing the time series of  $C_L$  for the two separate parts of the cylinder, i.e. upper

cylinder and base column, between the two cases. The lift coefficient for the individual parts are defined in a similar way to the whole cylinder by adopting the same overall projected area  $A_p$  in Eq. (4). For the cylinder at  $\theta = 0^\circ$ , the variation amplitude of  $C_L$  of the upper cylinder is almost twice that of the base column. For the inclined cylinder, however,  $C_L$  of the two parts are comparable in terms of amplitude. Comparing the two cases reveals that although  $C_L$  of the base column for the case with  $\theta = -10^\circ$  is smaller than that with  $\theta = 0^\circ$ , the upper cylinder is influenced by the inclination to an even larger extent, with  $C_L$  for the upright cylinder being significantly larger than its inclined counterpart. Additionally, nonlinear effects seem to be more pronounced for  $C_L$  of the upper part of the cylinder at  $\theta = -10^\circ$ . An FFT analysis is thus performed on the time series of  $C_L$  of the upper cylinder and the obtained magnitude of each frequency component between the two cases is compared in Figure 24. The forced vibration frequency  $f_n$  is utilised to normalise the frequency of the fluid forces. Results from both cases clearly exhibit a noteworthy and similar third-order frequency component, which is likely to be associated with the presence of the base column. Nevertheless, the considerable decrease in the magnitude of the first-order frequency component for the inclined case compared to its upright counterpart corroborates the increased nonlinearity in  $C_L$  for the cylinder at  $\theta = -10^\circ$  illustrated in Figure 23(a).

### 6.3.2 Pressure coefficient

The discrepancies in  $C_L$  between the two cases can be attributed to the differences in the fluid flow disturbed by the cylinder vibration. Figure 25 shows the comparison of the temporal and spatial distributions of the pressure coefficient  $C_p$  between the upright cylinder (solid black line) and its inclined counterpart (dashed black line). The same three sections previously examined in the stationary study in Section 6.1, i.e.  $z/L = 0.1, 0.25$  and  $0.5$ , are selected for the forced vibration cases. Each of the eight rows in Figure 25 corresponds to one instant marked in Figure 21 and Figure 23(a). The cylinder is represented as a grey circle, which also serves as a reference line for  $C_p = 0$ . It is thus defined that  $C_p$  is positive outside the grey circle and is negative inside it, and that the magnitude of  $C_p$  is proportional to the distance measured from the grey circle. One prominent feature of  $C_p$  in Figure 25 is the periodic movement of the high-pressure region on the front side of the cylinder sections at different instants, which is

caused by the variation of relative flow direction associated with the cylinder vibration. By comparing the results from the three sections, it is noted that the differences in  $C_p$  between the two cases at  $z/L=0.1$ , i.e. on the base column, are relatively small throughout the whole vibration cycle. By contrast, noticeable disparities between the upright and inclined cylinders are observed for the other two sections, which are located on the upper cylinder. This is consistent with the finding in Figure 23 that the inclination of the cylinder exerts more influence on the upper cylinder than on the base column.

A closer look into the results at  $z/L=0.25$  and  $0.5$  reveals that the most significant differences between the two cases occur at instants ‘C’ (also ‘D’) and ‘G’ (also ‘H’) when the cylinder vibration reaches its maximum in either direction and begins to move to the opposite side as can be seen from Figure 21. Additionally, the differences are most noticeable on the back side of the cylinder surface relative to its vibration velocity. Taking instant ‘C’ for example when the cylinder moves to its maximum in the positive  $y$  direction, when viewed from the sectional plane  $C_p$  on the lower half of the inclined cylinder is considerably larger in terms of magnitude than its upright counterpart. By contrast, the two curves nearly coincide with each other on the upper half. A larger negative  $C_p$  on the lower half of the inclined cylinder indicates an increase in the so-called suction force pointing towards the negative  $y$  direction and consequently leads to a smaller overall  $C_L$  in the positive  $y$  direction, which explains the large gap between the two cases at instant ‘C’ in Figure 23(a). The streamlines coloured by the non-dimensional streamwise velocity  $U_x/U$  at instant ‘C’ when viewed from the  $xoz$  plane are illustrated in Figure 26. It is found that the inclination greatly alters the fluid flow close to the rear side of the upper cylinder, which corroborates the discrepancies in  $C_p$  between the cylinder with two different inclination angles at instant ‘C’.

## 7 Conclusions

In this paper, the effect of inclination on the VIV of an elastically mounted rigid circular cylinder with a base column in a uniform flow at  $Re=300$  is investigated numerically. The cylinder has a low aspect ratio of  $L/D=2$  and a mass ratio of  $m^*=1$ , with no structural damping considered. Cylinders with two relatively small inclination angles, i.e.  $\theta=-5^\circ$  and  $\theta=-10^\circ$ , are studied along with an upright cylinder. Results

are compared and analysed under the stationary, free vibration and forced vibration conditions. Conclusions are presented as follows.

Although the overall force coefficients under the stationary condition are almost the same between the upright and inclined cases, the inclination of the cylinder leads to the differences in the distribution of pressure coefficient on spanwise sections near the base column. Meanwhile, due to the presence of the base column, the VIV response of the inclined cylinder deviates from the result of the upright cylinder at a relatively small inclination angle of  $\theta = -10^\circ$ , with a noticeable increase of about 20% in the maximum response amplitude. Additionally, the  $V_r$  range of the lock-in regime narrows for the inclined cylinder at  $\theta = -10^\circ$  compared to its upright counterpart due to the early transition of its response to the desynchronised regime. Considerable differences are also observed in the effective added mass between the cases, which is consistent with the discrepancies in the response frequency ratio. Moreover, forced vibration studies clearly demonstrate the significant impacts of inclination on the flow and fluid forces. It is found that the inclination affects the flow around the upper cylinder more than the base column. A considerable decrease in the amplitude of the lift coefficient on the upper cylinder is noted for the inclined cylinder compared to its upright counterpart, which is analysed in detail and explained by the temporal variation of the pressure coefficient distribution on the cylinder surface.

Results from the present study suggest that wind-induced inclination may exert great impacts on the vortex-induced motion of FOWTs in current and thus should be taken into account during the design phase. At this stage, wind and current are assumed to be aligned in the same direction. However, in real-world scenarios it is very likely that they propagate in different directions, thus leading to various inclination directions. Additionally, only the transverse response of the cylinder is considered in the present study while the significant differences observed in the drag coefficient between the upright and inclined cases imply that the inclination of the cylinder may affect its inline response as well. As a result, the effects of inclination direction and two-degree-of-freedom VIV are worth detailed investigations and will be analysed in future studies.

## Acknowledgements

This work was supported by the National Natural Science Foundation of China (Grant Nos. 51909255, U1806229 and 51779237). The authors would also like to acknowledge the Center for High Performance Computing and System Simulation, Pilot National Laboratory for Marine Science and Technology (Qingdao), for kindly providing access to its HPC facility.

## References

- Antonutti R, Peyrard C, Johanning L, Incecik A, Ingram D (2014). An investigation of the effects of wind-induced inclination on floating wind turbine dynamics: heave plate excursion. *Ocean Engineering*, **91**, 208-217.
- Antonutti R, Peyrard C, Johanning L, Incecik A, Ingram D (2016). The effects of wind-induced inclination on the dynamics of semi-submersible floating wind turbines in the time domain. *Renewable Energy*, **88**, 83-94.
- Bearman PW (1984). Vortex Shedding from Oscillating Bluff Bodies. *Annual Review of Fluid Mechanics*, **16**(1), 195-222.
- Bearman PW (2011). Circular cylinder wakes and vortex-induced vibrations. *Journal of Fluids and Structures*, **27**(5), 648-658.
- Benitz MA, Carlson DW, Seyed-Aghazadeh B, Modarres-Sadeghi Y, Lackner MA, Schmidt DP (2016). CFD simulations and experimental measurements of flow past free-surface piercing, finite length cylinders with varying aspect ratios. *Computers & Fluids*, **136**, 247-259.
- Bourdier S, Chaplin JR (2012). Vortex-induced vibrations of a rigid cylinder on elastic supports with end-stops, Part 1: Experimental results. *Journal of Fluids and Structures*, **29**, 62-78.
- Dahl JM, Hover FS, Triantafyllou MS, Oakley OH (2010). Dual resonance in vortex-induced vibrations at subcritical and supercritical Reynolds numbers. *Journal of Fluid Mechanics*, **643**, 395-424.
- Franzini GR, Gonçalves RT, Meneghini JR, Fujarra ALC (2013). One and two degrees-of-freedom Vortex-Induced Vibration experiments with yawed cylinders. *Journal of Fluids and Structures*, **42**, 401-420.
- Gonçalves RT, Meneghini JR, Fujarra ALC (2018). Vortex-induced vibration of floating circular cylinders with very low aspect ratio. *Ocean Engineering*, **154**, 234-251.
- Gsell S, Bourguet R, Braza M (2019). One- versus two-degree-of-freedom vortex-induced vibrations of a circular cylinder at  $Re=3900$ . *Journal of Fluids and Structures*, **85**, 165-180.
- Hover FS, Davis JT, Triantafyllou MS (2004). Three-dimensionality of mode transition in vortex-induced vibrations of a circular cylinder. *European Journal of Mechanics - B/Fluids*, **23**(1), 29-40.

- Hu G, Li C, Tse KT, Kwok KCS (2018). Vortex induced vibration of an inclined finite-length square cylinder. *European Journal of Mechanics - B/Fluids*, **68**, 144-152.
- Jain A, Modarres-Sadeghi Y (2013). Vortex-induced vibrations of a flexibly-mounted inclined cylinder. *Journal of Fluids and Structures*, **43**, 28-40.
- Khalak A, Williamson CHK (1999). Motions, forces and mode transitions in vortex-induced vibrations at low mass damping. *Journal of Fluids and Structures*, **13**(7), 813-851.
- Kim J, Choi H (2005). Distributed forcing of flow over a circular cylinder. *Physics of Fluids*, **17**(3), 033103.
- Liu F, Fu Q, Tian Z (2019a). A Laplace-domain method for motion response estimation of floating structures based on a combination of generalised transfer function and partial fraction. *Ships and Offshore Structures*, 1-15.
- Liu F, Gao S, Han H, Tian Z, Liu P (2019b). Interference reduction of high-energy noise for modal parameter identification of offshore wind turbines based on iterative signal extraction. *Ocean Engineering*, **183**, 372-383.
- Liu Y, Liu F, Wang E, Xiao Q, Li L (2020). The effect of base column on vortex-induced vibration of a circular cylinder with low aspect ratio. *Ocean Engineering*, **196**, 106822.
- Liu Y, Xiao Q, Incecik A, Peyrard C, Wan D (2017). Establishing a fully coupled CFD analysis tool for floating offshore wind turbines. *Renewable Energy*, **112**, 280-301.
- Lucor D, Karniadakis GE (2003). Effects of Oblique Inflow in Vortex-Induced Vibrations. *Flow, Turbulence and Combustion*, **71**(1), 375-389.
- Matsuzaki K, Shingai M, Haramoto Y, Munekata M, Ohba H (2004). Visualization of three-dimensional flow structures in the wake of an inclined circular cylinder. *Journal of Visualization*, **7**(4), 309-316.
- Morse TL, Govardhan RN, Williamson CHK (2008). The effect of end conditions on the vortex-induced vibration of cylinders. *Journal of Fluids and Structures*, **24**(8), 1227-1239.
- Morse TL, Williamson CHK (2009). The effect of Reynolds number on the critical mass phenomenon in vortex-induced vibration. *Physics of Fluids*, **21**(4), 045105.
- Navrose, Mittal S (2013). Free vibrations of a cylinder: 3-D computations at Re=1000. *Journal of Fluids and Structures*, **41**, 109-118.
- Newmark NM (1959). A method of computation for structural dynamics. *Journal of the Engineering Mechanics Division*, **85**(3), 67-94.
- Raghavan K, Bernitsas MM (2011). Experimental investigation of Reynolds number effect on vortex induced vibration of rigid circular cylinder on elastic supports. *Ocean Engineering*, **38**(5), 719-731.
- Ramberg SE (1983). The effects of yaw and finite length upon the vortex wakes of stationary and vibrating circular cylinders. *Journal of Fluid Mechanics*, **128**, 81-107.
- Robertson A, Jonkman J, Masciola M, Song H, Goupee A, Coulling A, Luan C. Definition of the semisubmersible floating system for phase II of OC4. 2014.

- Sarpkaya T (2004). A critical review of the intrinsic nature of vortex-induced vibrations. *Journal of Fluids and Structures*, **19**(4), 389-447.
- Thakur A, Liu X, Marshall JS (2004). Wake Flow of Single and Multiple Yawed Cylinders. *Journal of Fluids Engineering*, **126**(5), 861-870.
- Tian Z, Liu F, Zhou L, Yuan C (2020). Fluid-structure interaction analysis of offshore structures based on separation of transferred responses. *Ocean Engineering*, **195**, 106598.
- Wang E, Xiao Q, Incecik A (2017). Three-dimensional numerical simulation of two-degree-of-freedom VIV of a circular cylinder with varying natural frequency ratios at  $Re=500$ . *Journal of Fluids and Structures*, **73**, 162-182.
- Wang E, Xu W, Gao X, Liu L, Xiao Q, Ramesh K (2019). The effect of cubic stiffness nonlinearity on the vortex-induced vibration of a circular cylinder at low Reynolds numbers. *Ocean Engineering*, **173**, 12-27.
- Williamson CHK, Govardhan R (2004). VORTEX-INDUCED VIBRATIONS. *Annual Review of Fluid Mechanics*, **36**(1), 413-455.
- Zhao M (2015a). Numerical simulation of vortex-induced vibration of a circular cylinder in a spanwise shear flow. *Physics of Fluids*, **27**(6), 063101.
- Zhao M (2015b). The validity of the independence principle applied to the vortex-induced vibration of an inclined cylinder in steady flow. *Applied Ocean Research*, **53**, 155-160.
- Zhao M, Cheng L (2014). Vortex-induced vibration of a circular cylinder of finite length. *Physics of Fluids*, **26**(1), 015111-1-26.
- Zhao M, Cheng L, Zhou T (2009). Direct numerical simulation of three-dimensional flow past a yawed circular cylinder of infinite length. *Journal of Fluids and Structures*, **25**(5), 831-847.

Table 1 Results of mesh and time-step size sensitivity tests at  $\theta = -10^\circ$  and  $V_r = 6$ :  
 $N_c$  – number of elements along cylinder circumference;  $\Delta t$  – time-step size;  $T_v$  –  
vortex shedding period for a stationary, infinitely long cylinder

Mesh	Cell count	$N_c$	$\Delta t/T_v$	$A_y/D$	$C_{L,rms}$
Coarse	307,965	60	1/1000	0.6910	0.3686
Medium	631,000	80	1/500	0.6902	0.3588
			1/1000	0.6874	0.3580
			1/2000	0.6862	0.3580
Fine	1,119,780	100	1/1000	0.6876	0.3517

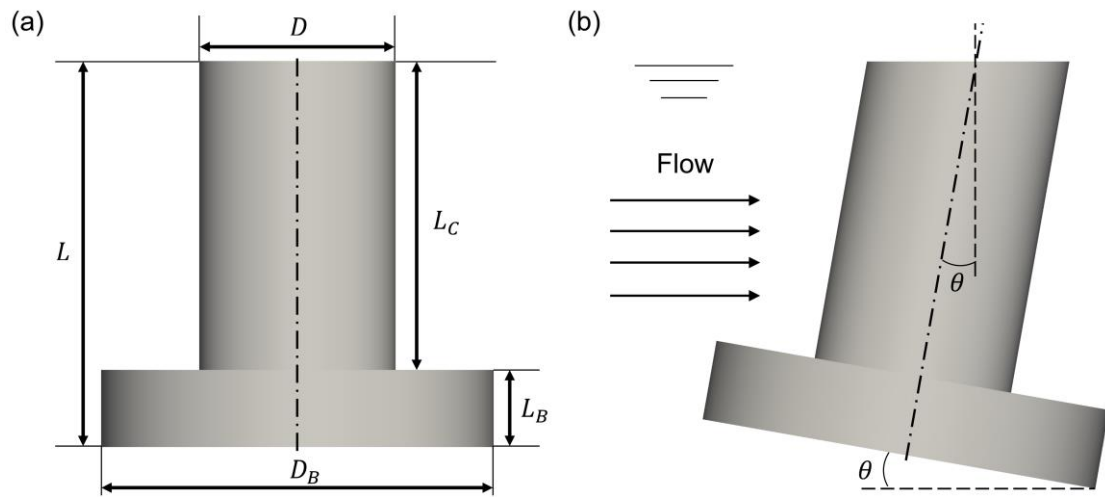


Figure 1 Schematic diagram of (a) geometry and (b) inclination for a circular cylinder with a base column:  $L$  – overall length of cylinder;  $D$  – diameter of upper cylinder;  $L_C$  – length of upper cylinder;  $D_B$  – diameter of base column;  $L_B$  – length of base column;  $\theta$  – inclination angle

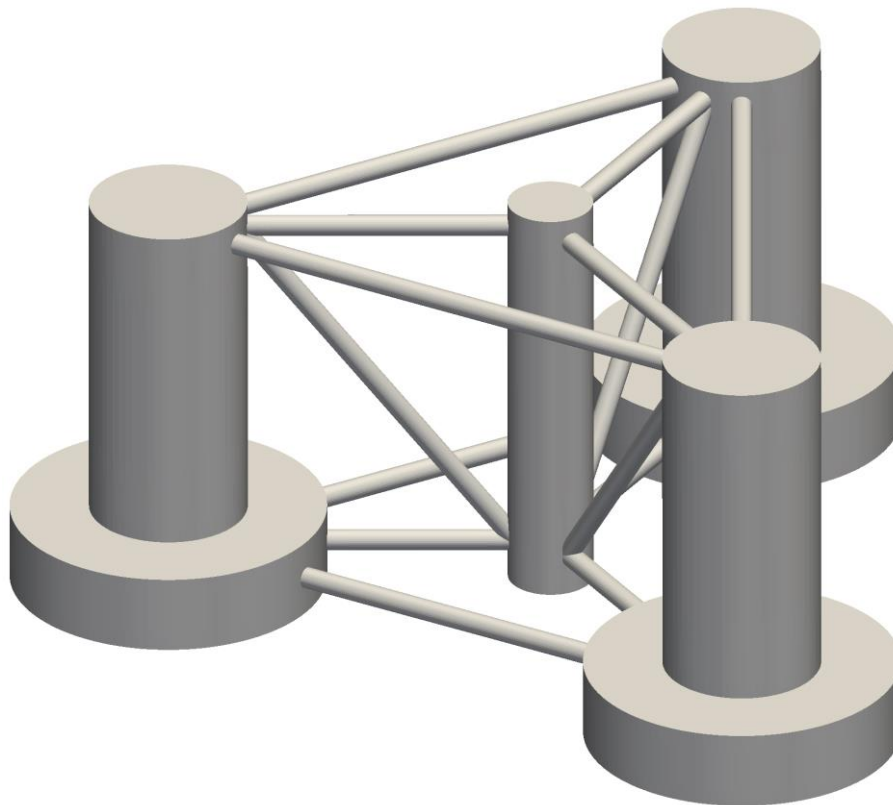


Figure 2 Illustration of DeepCwind semi-submersible platform for OC4 FOWT

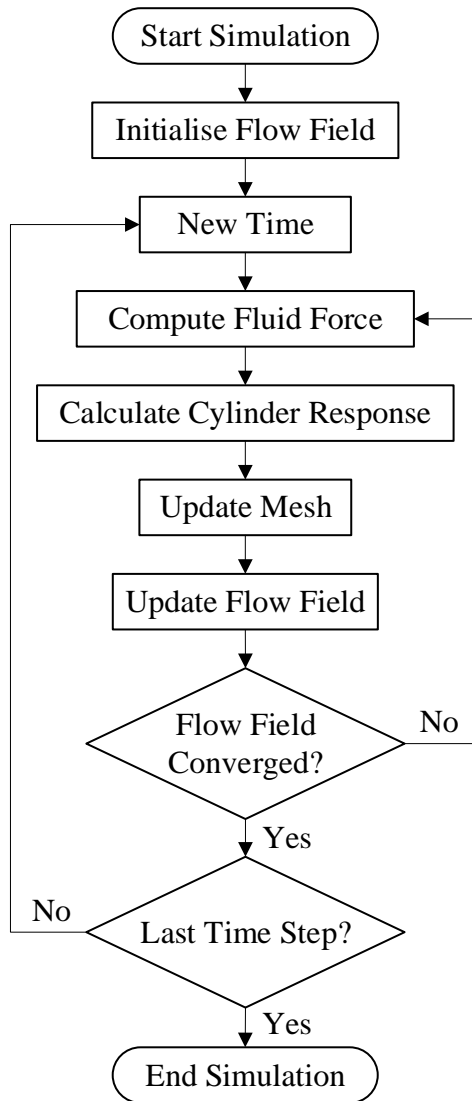


Figure 3 Flow chart of fluid-structure interaction

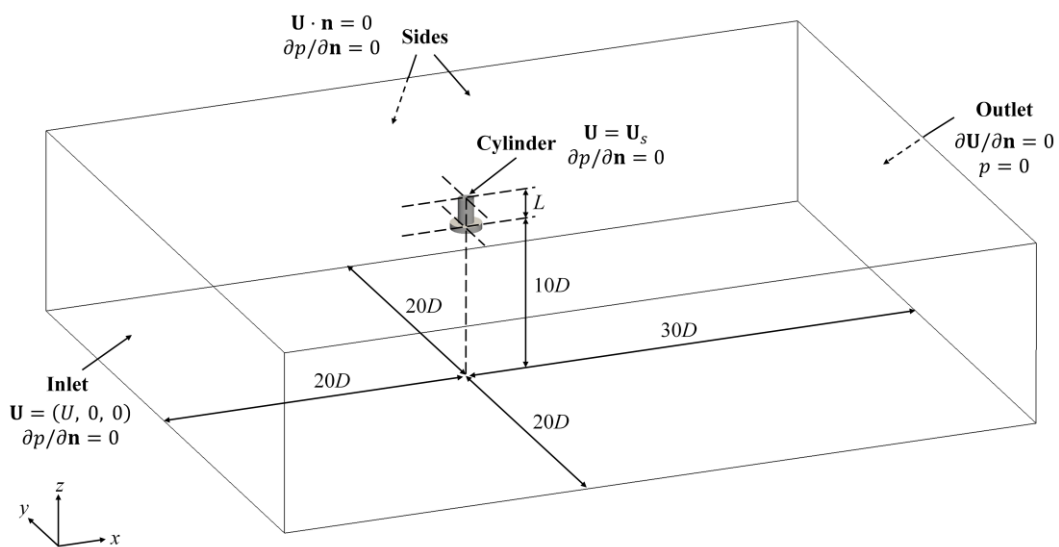


Figure 4 Dimensions and boundary conditions for VIV simulation of an upright circular cylinder with a base column:  $L$  – overall length of cylinder;  $D$  – diameter of the upper cylinder

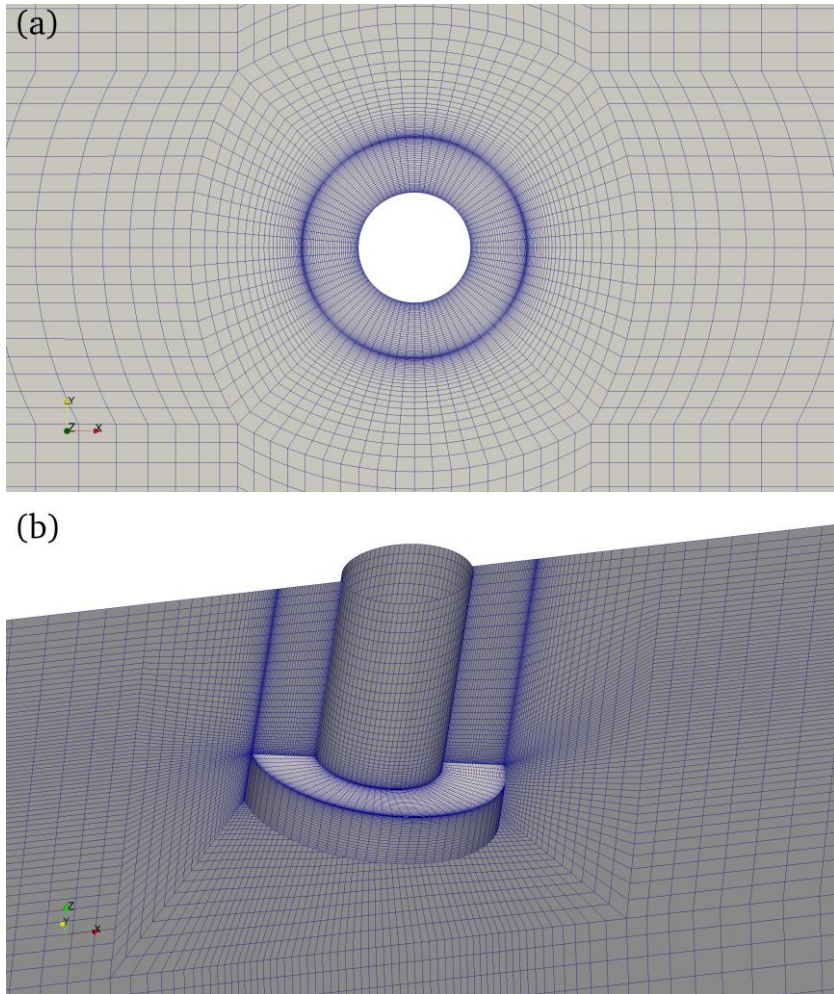


Figure 5 Computational mesh for VIV simulation of a circular cylinder with a base column at  $\theta = -10^\circ$ : (a) top side; (b) cylinder surface

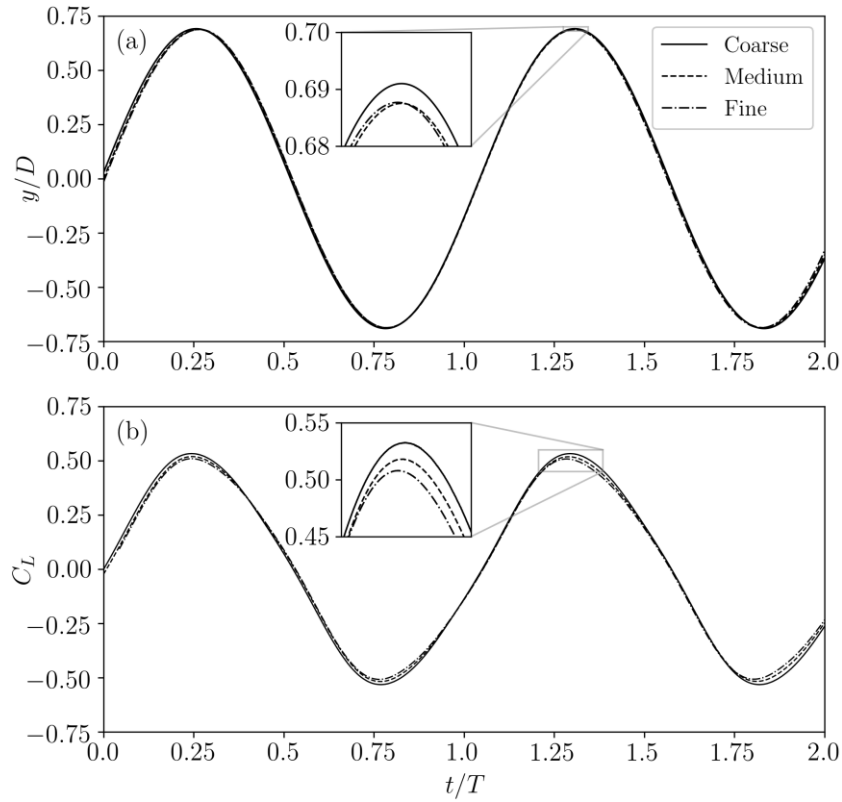


Figure 6 Comparison of time series of (a) VIV response  $y/D$  and (b) lift coefficient  $C_L$  for cases with different mesh density at  $\theta = -10^\circ$  and  $V_r = 6$

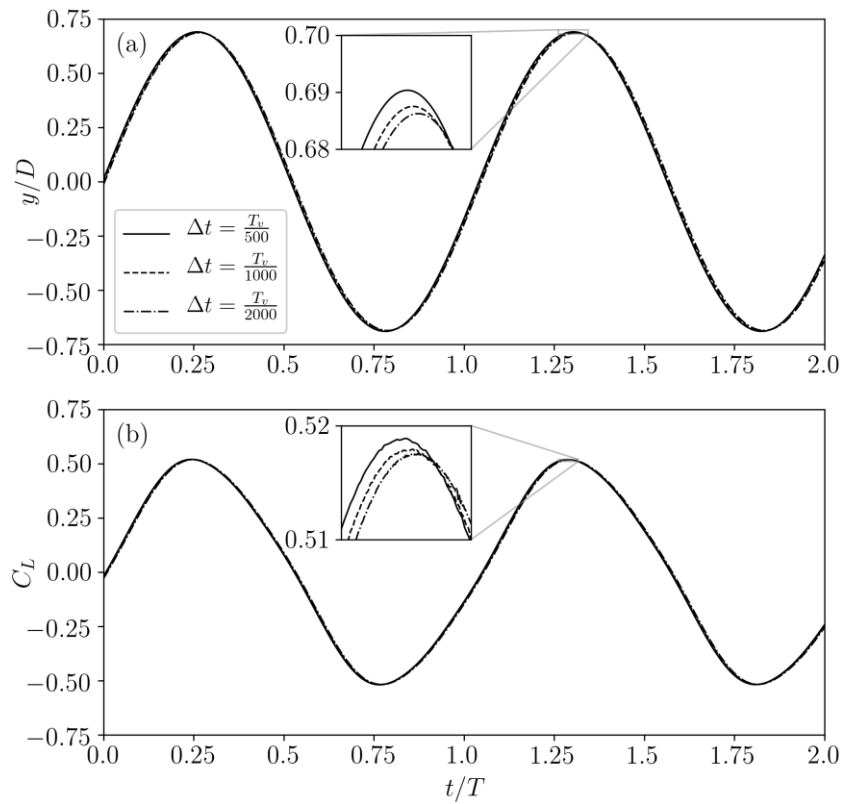


Figure 7 Comparison of time series of (a) VIV response  $y/D$  and (b) lift coefficient  $C_L$  for cases with different time-step size at  $\theta = -10^\circ$  and  $V_r = 6$

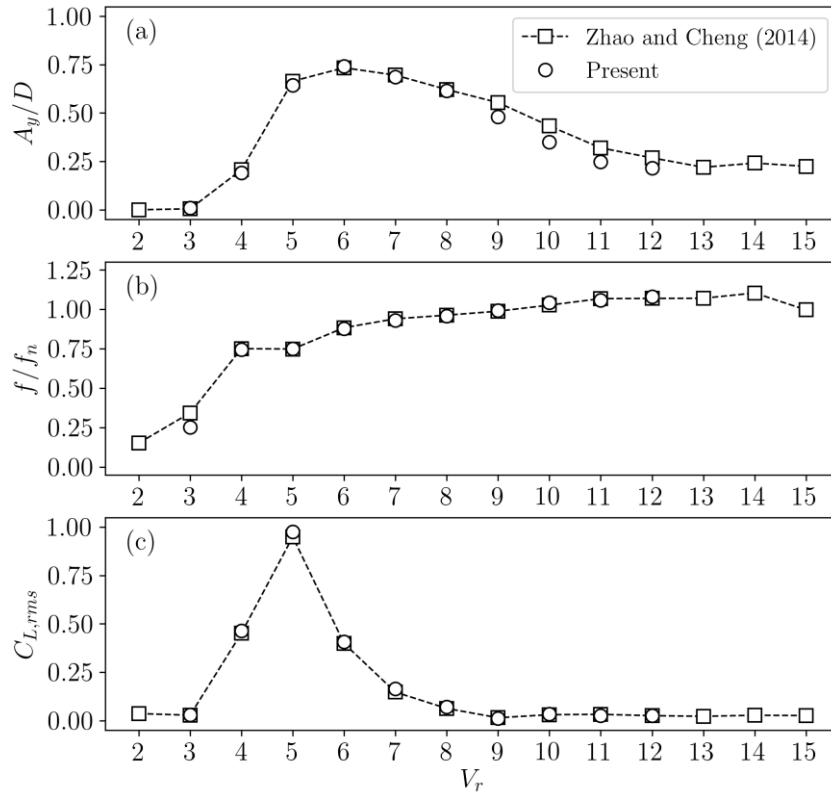


Figure 8 Comparison of (a) response amplitude  $A_y/D$ , (b) response frequency ratio  $f/f_n$  and (c) rms of lift coefficient  $C_{L,rms}$  of VIV of a truncated cylinder with  $L/D = 2$  at  $Re = 300$

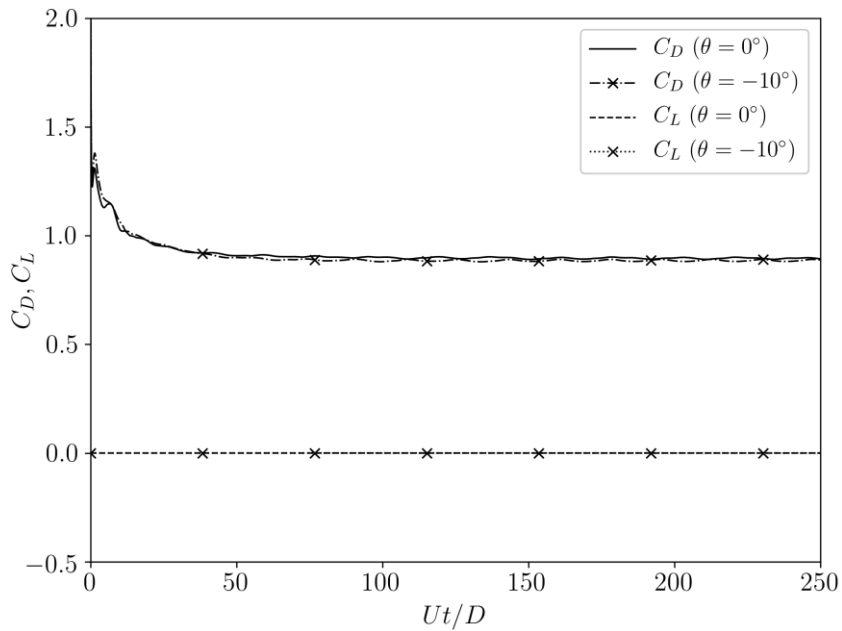


Figure 9 Comparison of time series of force coefficients for a stationary cylinder at  $\theta = 0^\circ$  and  $\theta = -10^\circ$

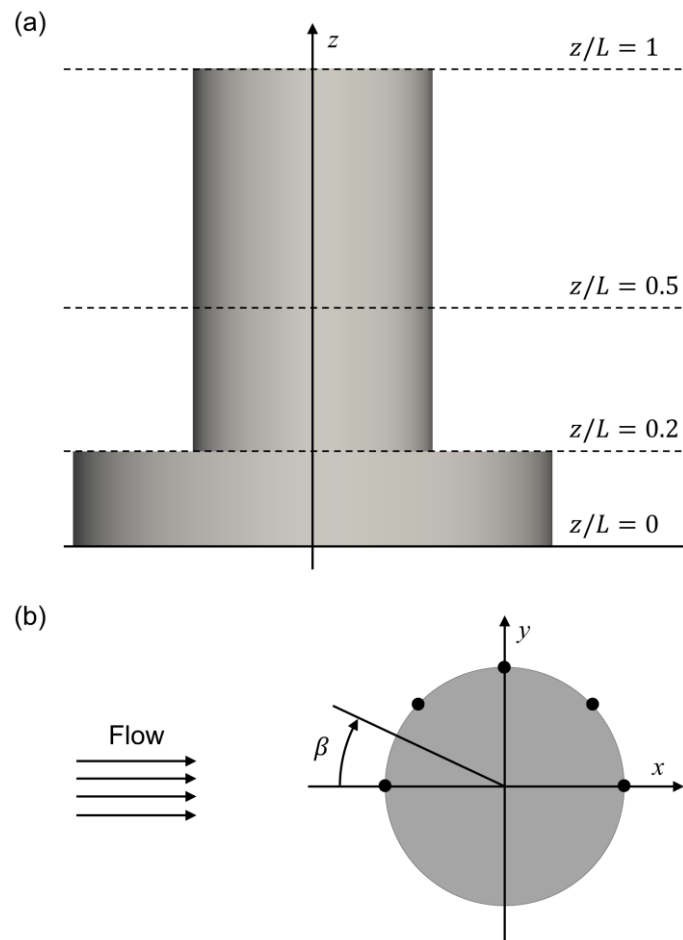


Figure 10 Schematic diagram of (a) sections along cylinder and (b) azimuth angle  $\beta$  at given section

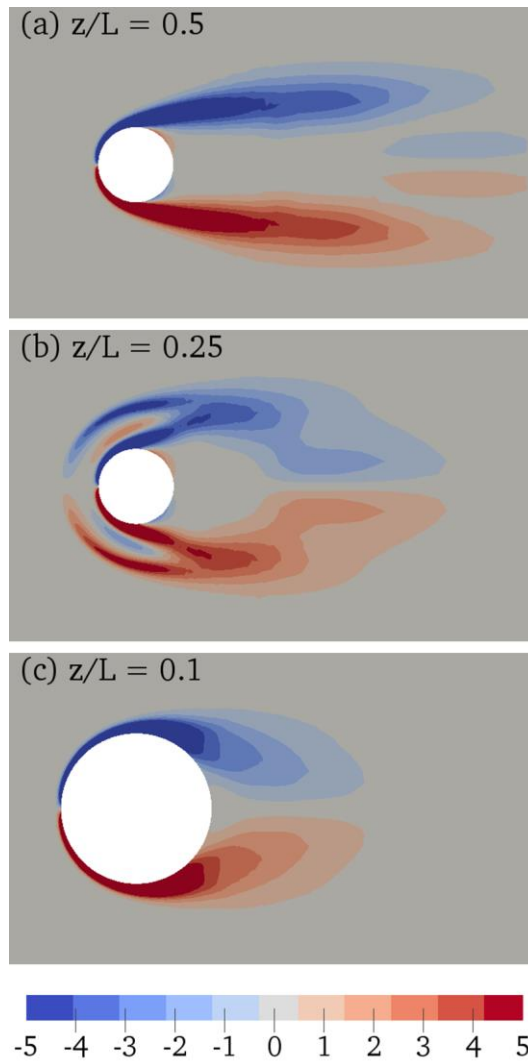


Figure 11 Contours of axial vorticity  $\omega_z$  at three sections along a stationary cylinder at  $\theta = -10^\circ$

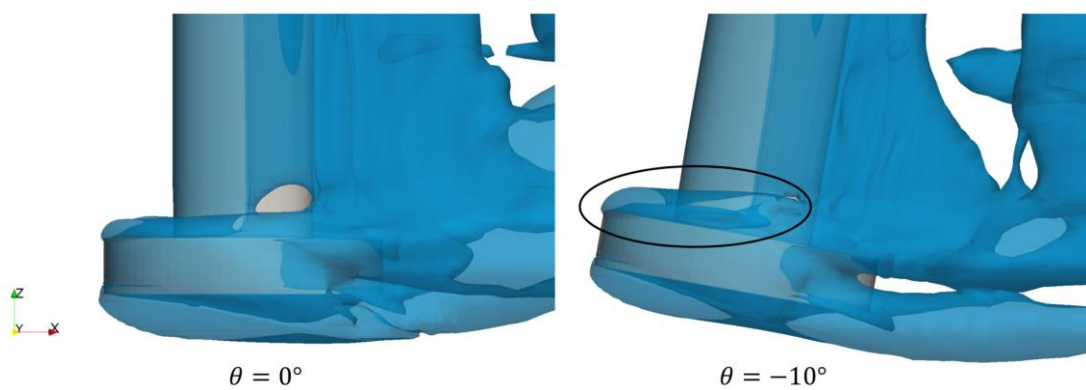


Figure 12 Comparison of vortex flow represented by iso-surface of  $Q = 0.2$  for a stationary cylinder at  $\theta = 0^\circ$  and  $\theta = -10^\circ$

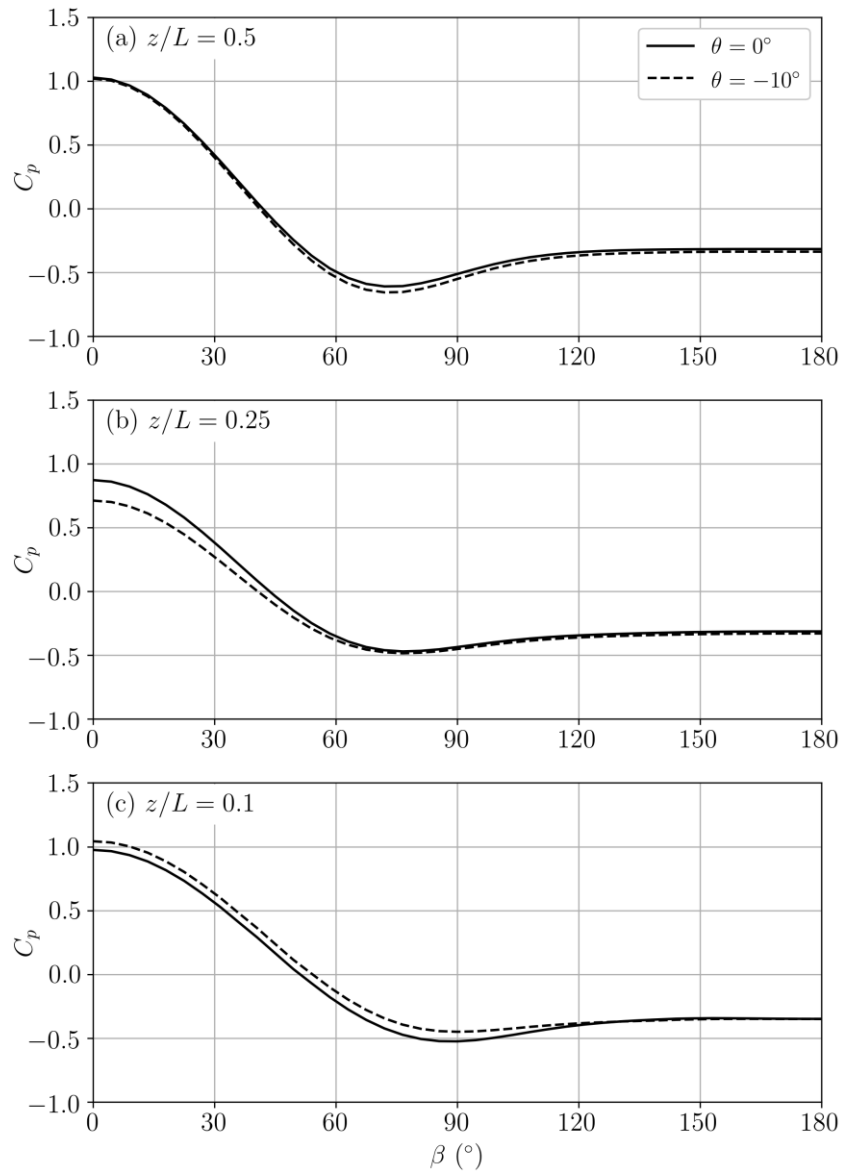


Figure 13 Comparison of distribution of pressure coefficient  $C_p$  with respect to azimuth angle  $\beta$  at three sections along a stationary cylinder at  $\theta = 0^\circ$  and  $\theta = -10^\circ$

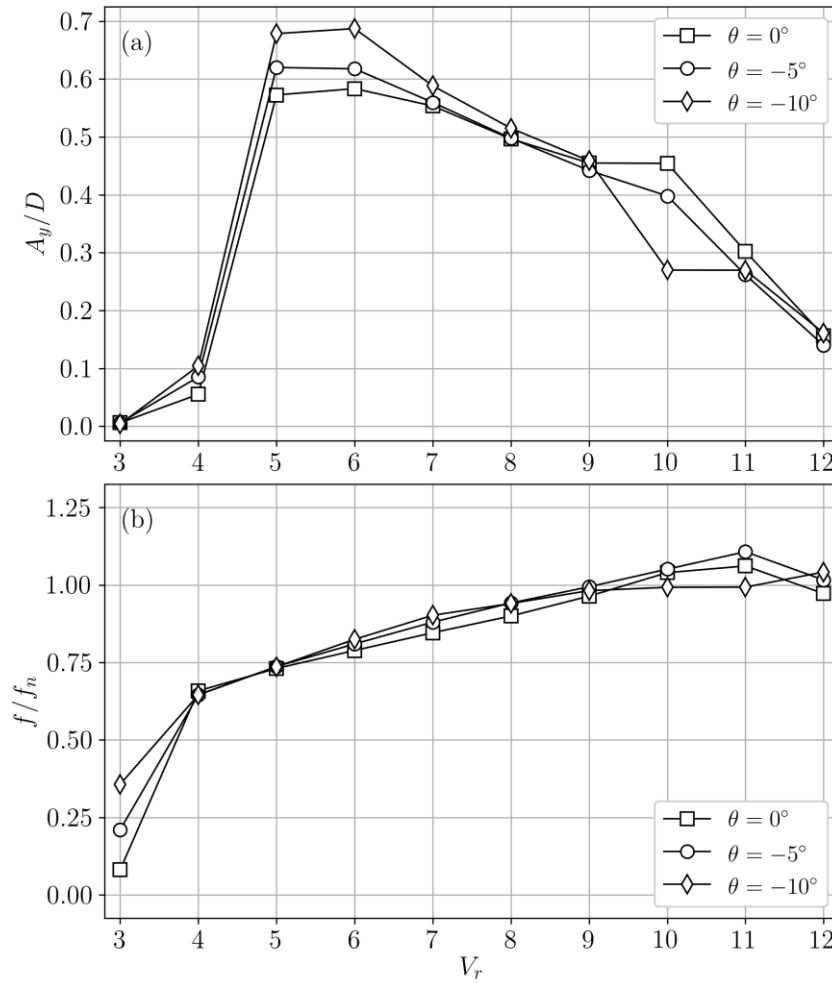


Figure 14 Comparison of (a) response amplitude  $A_y/D$  and (b) response frequency ratio  $f/f_n$  against  $V_r$  for VIV of a cylinder with different inclination angles

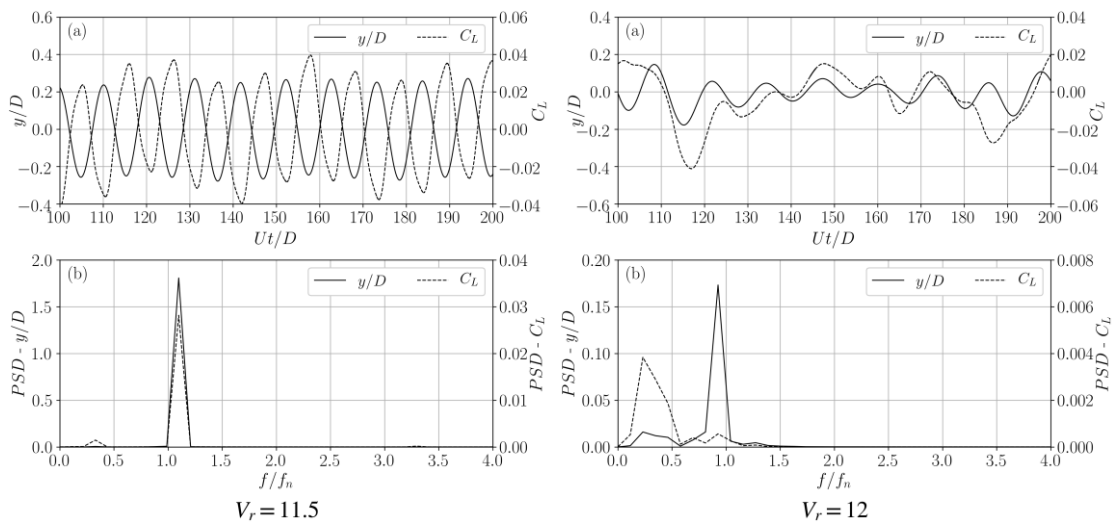


Figure 15 (a) Time series and (b) PSD of response  $y/D$  and lift coefficient  $C_L$  for VIV of a cylinder at  $\theta = 0^\circ$ ,  $V_r = 11.5$  and  $V_r = 12$

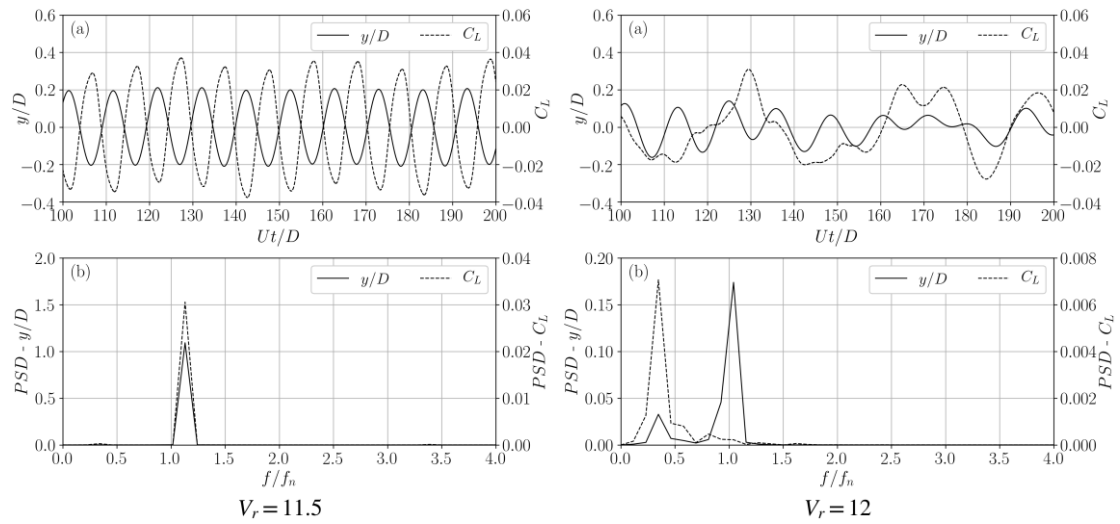


Figure 16 (a) Time series and (b) PSD of response  $y/D$  and lift coefficient  $C_L$  for VIV of a cylinder at  $\theta = -5^\circ$ ,  $V_r = 11.5$  and  $V_r = 12$

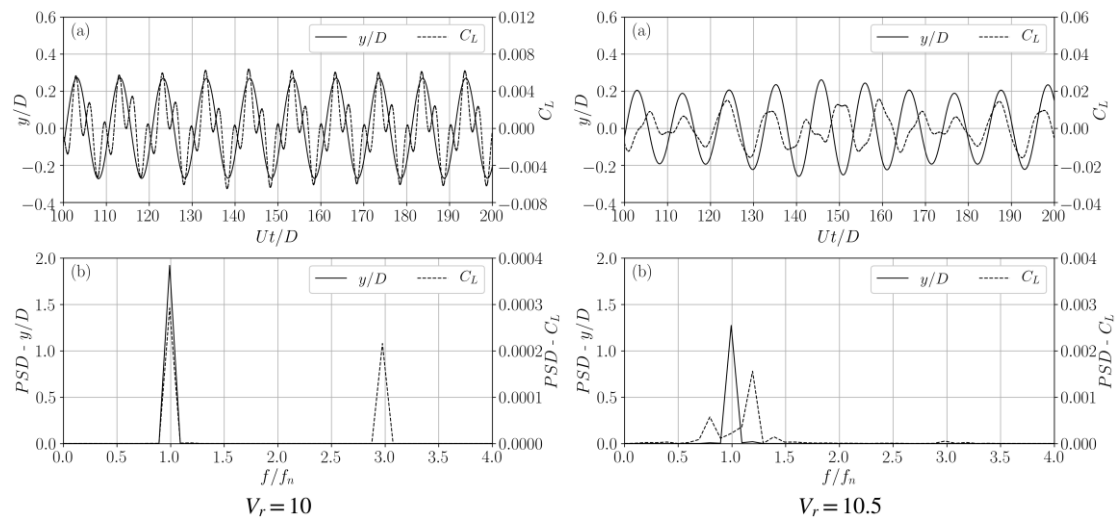


Figure 17 (a) Time series and (b) PSD of response  $y/D$  and lift coefficient  $C_L$  for VIV of a cylinder at  $\theta = -10^\circ$ ,  $V_r = 10$  and  $V_r = 10.5$

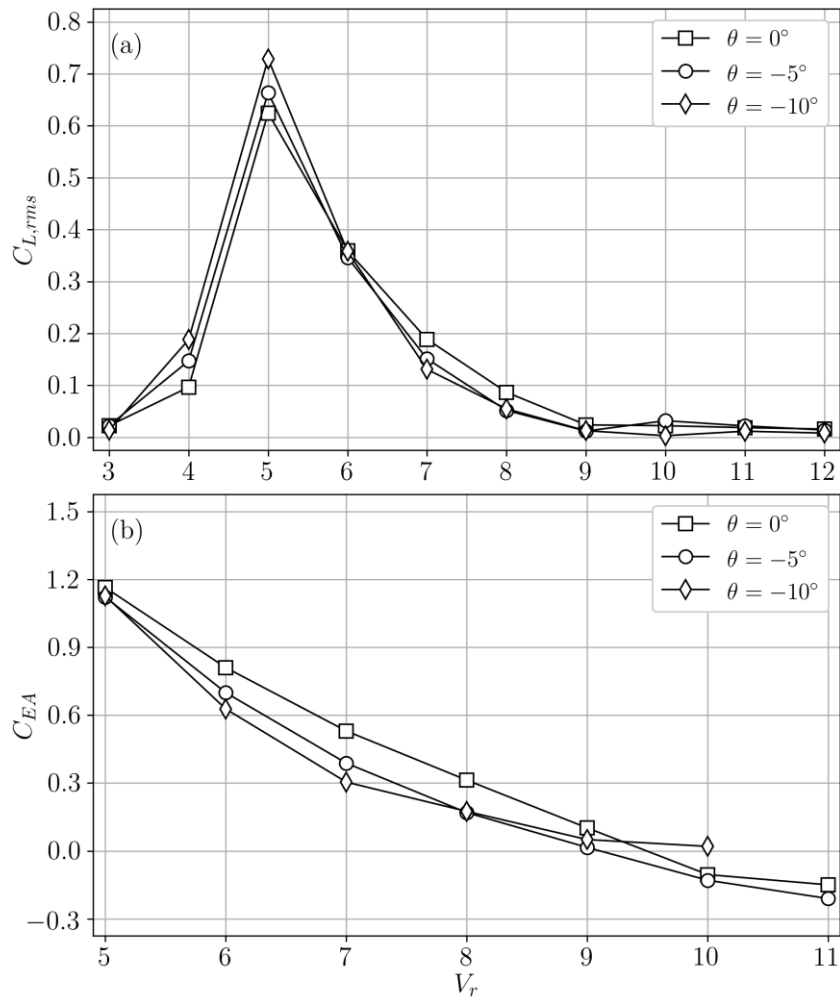


Figure 18 Comparison of (a) rms of lift coefficient  $C_{L,rms}$  and (b) effective added mass coefficient  $C_{EA}$  against  $V_r$  for VIV of a cylinder with different inclination angles

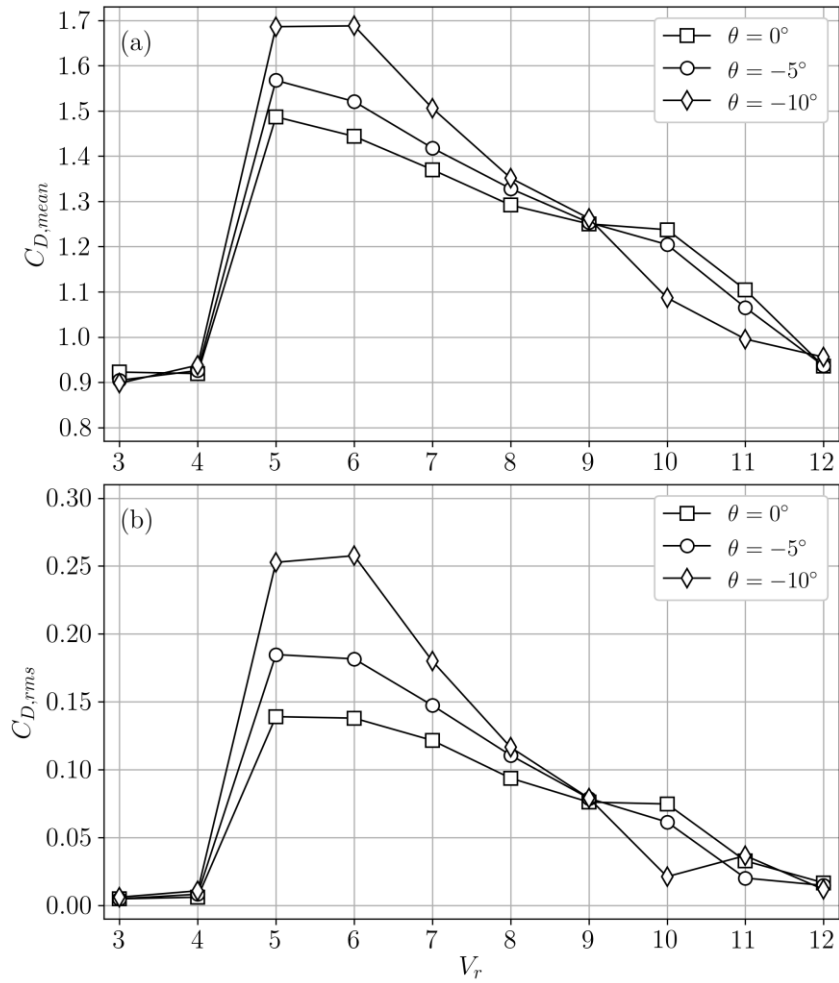


Figure 19 Comparison of (a) mean of drag coefficient  $C_{D,mean}$  and (b) rms of drag coefficient  $C_{D,rms}$  against  $V_r$  for VIV of a cylinder with different inclination angles

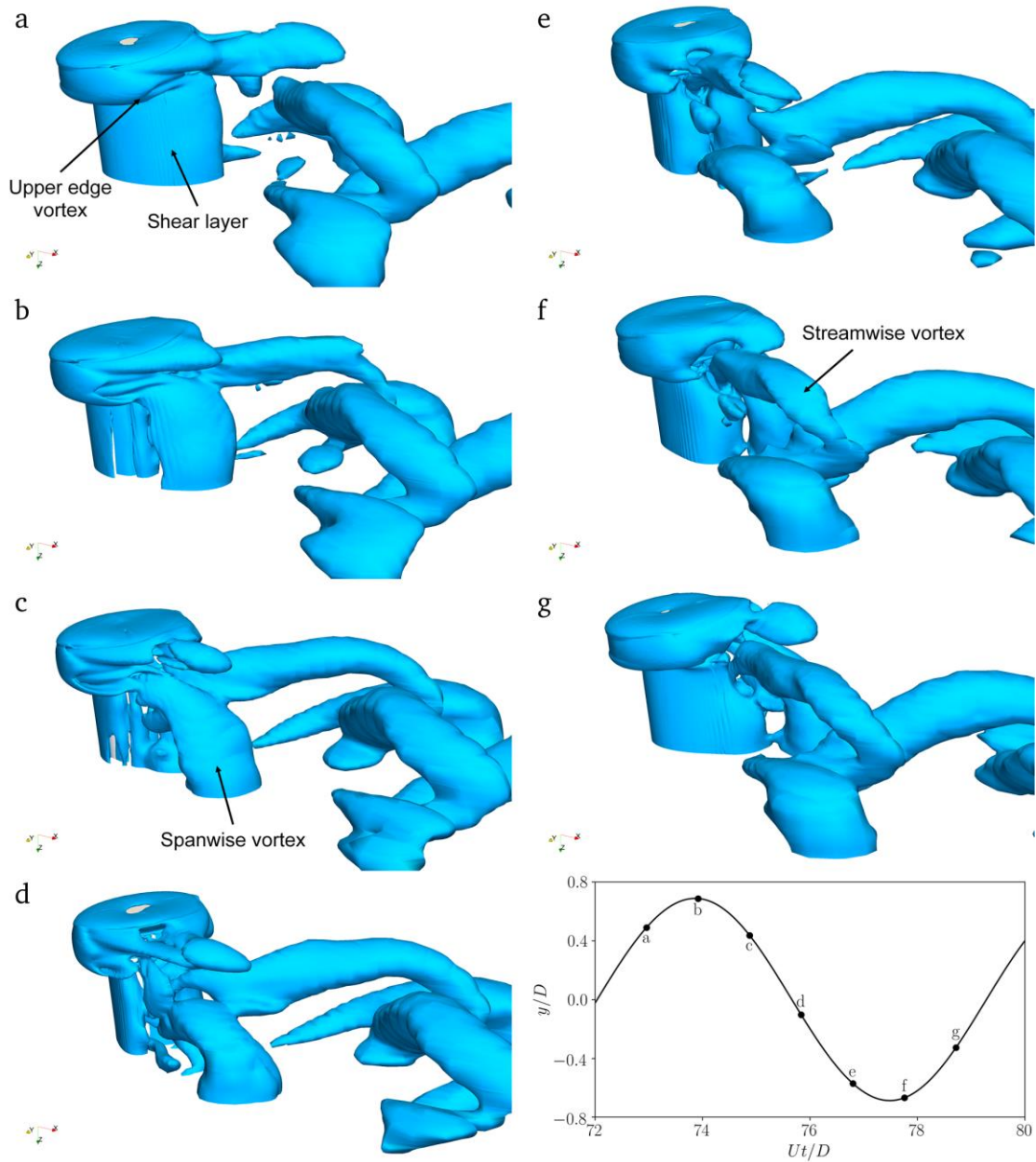


Figure 20 Vortex evolution represented by iso-surface of  $Q = 0.2$  for VIV of an inclined cylinder with  $\theta = -10^\circ$  at  $V_r = 6$  within one response cycle

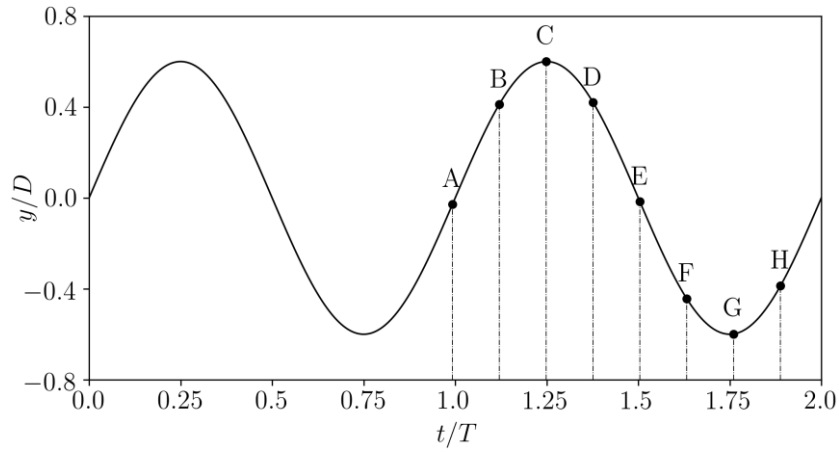


Figure 21 Time series of forced vibration  $y/D$  over two complete cycles

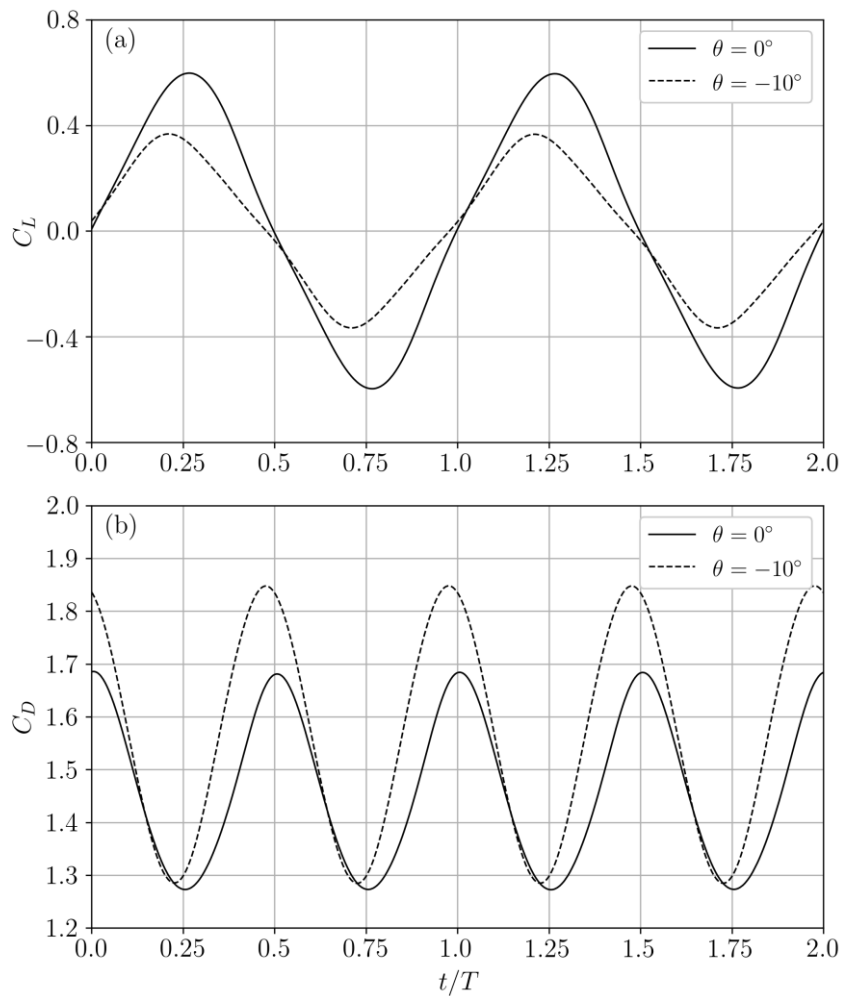


Figure 22 Comparison of time series of (a) lift coefficient  $C_L$  and (b) drag coefficient  $C_D$  for a cylinder with inclination angles of  $\theta = 0^\circ$  and  $\theta = -10^\circ$  under forced vibration

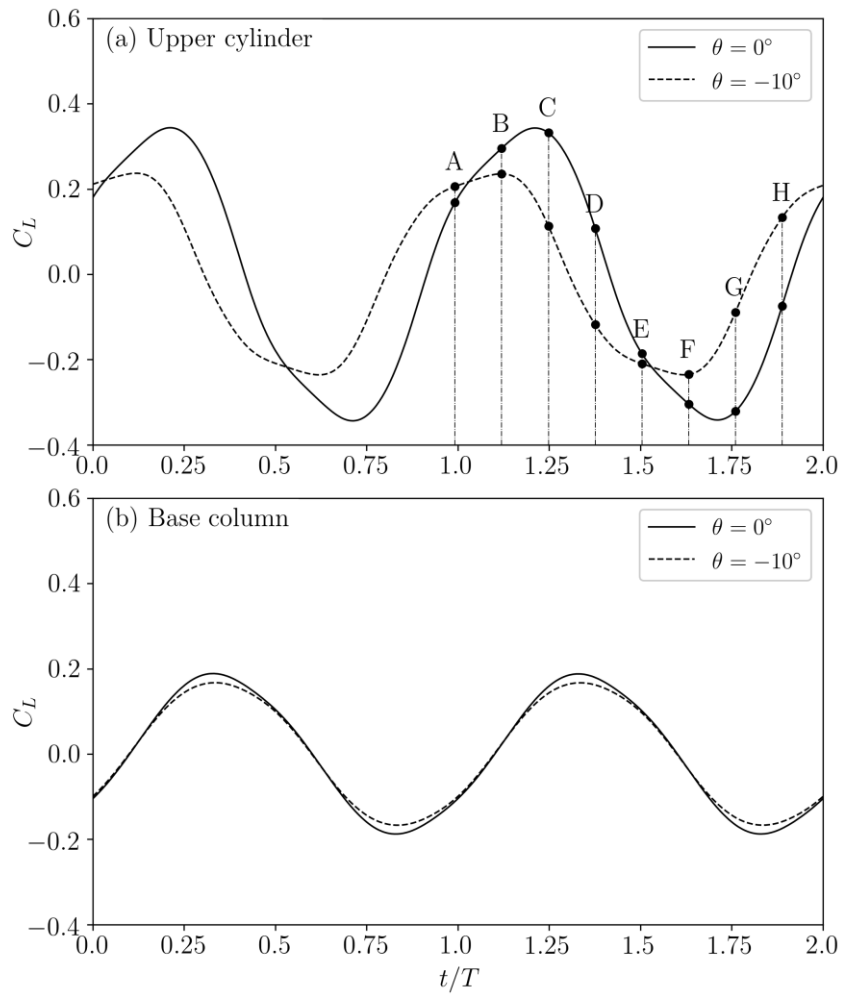


Figure 23 Comparison of time series of lift coefficient  $C_L$  for separate parts of a cylinder with inclination angles of  $\theta = 0^\circ$  and  $\theta = -10^\circ$  under forced vibration: (a) upper cylinder and (b) base column

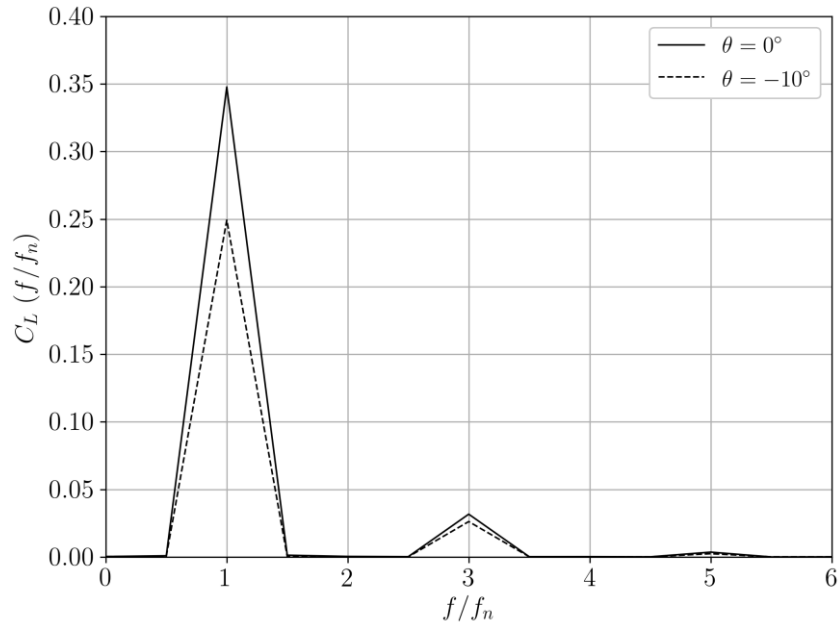


Figure 24 Comparison of FFT magnitude of lift coefficient  $C_L (f/f_n)$  for upper cylinder with inclination angles of  $\theta = 0^\circ$  and  $\theta = -10^\circ$  under forced vibration

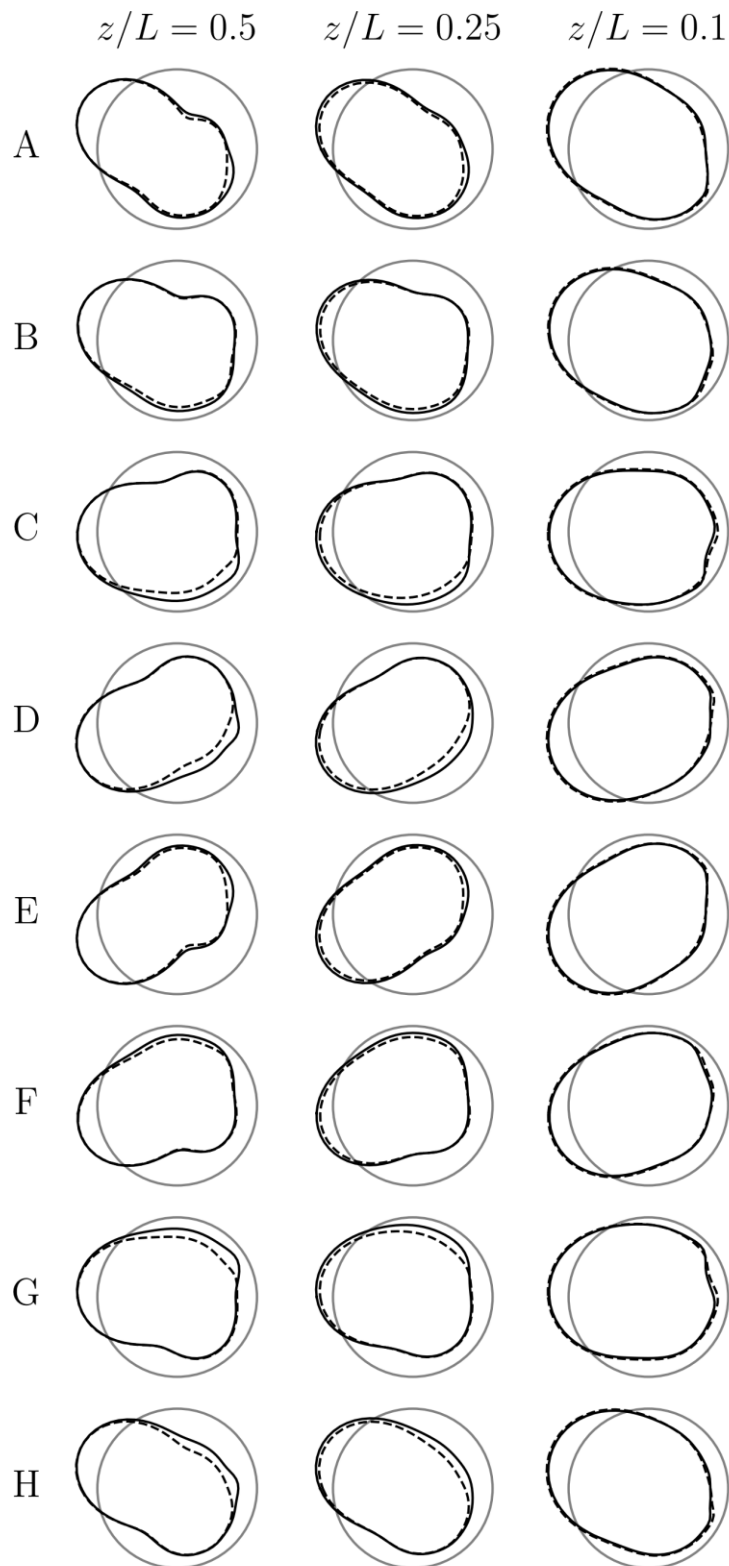


Figure 25 Comparison of distribution of pressure coefficient  $C_p$  at eight instants and three sections for a cylinder (grey circle) with inclination angles of  $\theta = 0^\circ$  (solid black line) and  $\theta = -10^\circ$  (dashed black line) under forced vibration: positive  $C_p$  outside cylinder and negative inside; magnitude of  $C_p$  proportional to distance measured from cylinder surface; incident flow from left to right

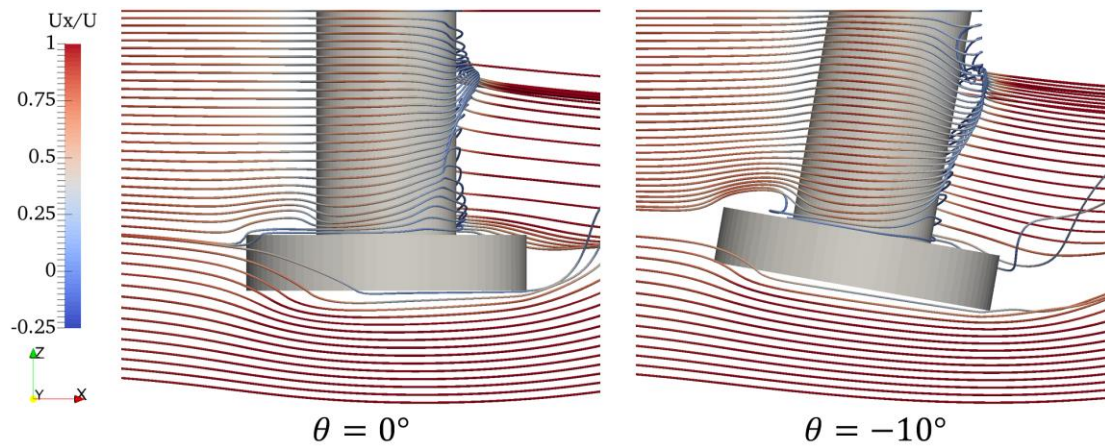


Figure 26 Comparison of streamlines at instant 'C' coloured by non-dimensional streamwise velocity  $U_x/U$  for a cylinder with inclination angles of  $\theta = 0^\circ$  and  $\theta = -10^\circ$  under forced vibration